Non-Equilibrium Coherent Transport in Mesoscopic Conductors

UNI BASEL

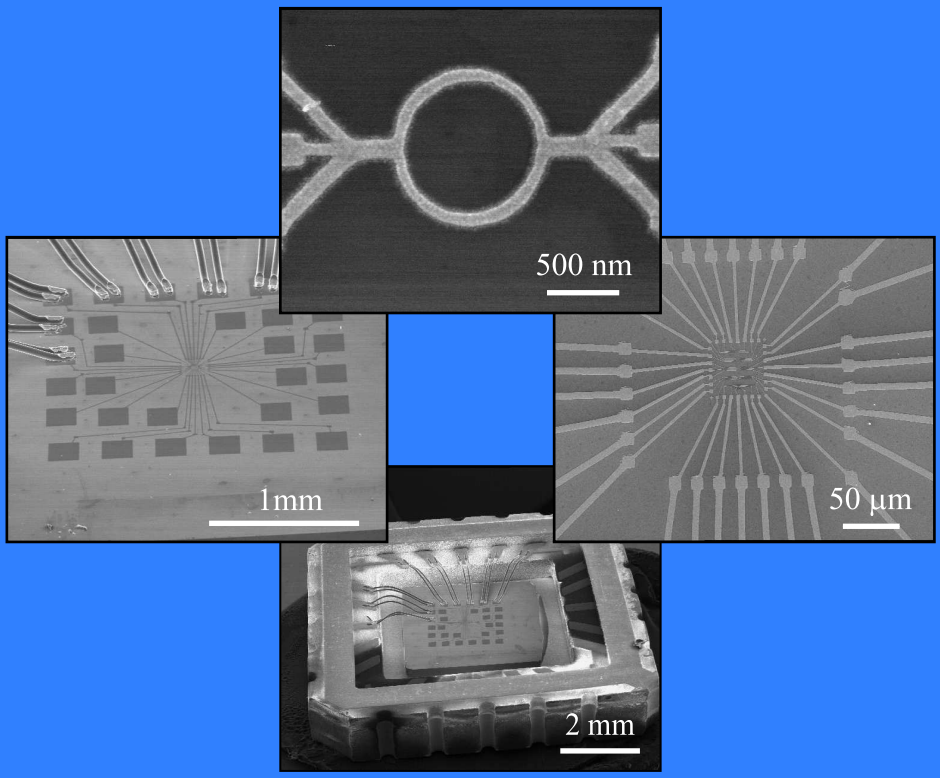

Christophe Terrier

PhD Thesis

Non-Equilibrium Coherent Transport in Mesoscopic Conductors

INAUGURALDISSERTATION
zur
Erlangung der Würde eines Doktors der Philosophie
vorgelegt der
Philosophisch-Naturwissenschaftlichen Fakultät
der Universität Basel
von

Christophe Terrier

aus Montignez (JU)

Bassecourt, 2002

Genehmigt von der Philosophisch-Naturwissenschaftlichen Fakultät
auf Antrag von:

Prof. Dr. C. Schönenberger
Prof. Dr. C. Bruder
Dr. U. Staufer

Basel, den 19. Dezember 2000

Prof. Dr. Andreas D. Zuberbühler

à Shih-Yi

Contents

Chapter 1

Introduction

In the last two decades there has been tremendous progress made in the development of technologies for reaching the physical limits of miniaturisation, in order to satisfy increasing industrial demands. Requirements for lower power consumption and faster processing speeds of electronic devices has imposed the necessity for smaller dimensions and has led to a rapid development of manufacturing technologies. Today, the critical dimension of 100 - 130 nm is reached in commercial microprocessors fabrication using optical lithographic techniques. This limit can be reduced to a few tens of nanometres by use of electron-beam lithography (EBL), electrochemical methods, etching techniques, etc. Another approach is promising for overcoming the technical limitations of the above mentioned methods for reducing the size of electronic circuits. Namely, under certain conditions natural microscopic components can be manipulated to bind themselves together, building well-defined geometrical arrangements comprising fullerene balls, DNA spirals, carbon nanotubes, etc. This self-assembly approach [1] for making useful electronic devices is a challenging task for scientists and engineers and will require extensive interdisciplinary work involving physics, chemistry and biology on the fundamental side, and micro-engineering disciplines on the application side.

The above mentioned technologies and techniques have opened another field of solid state science, namely the one of mesoscopic physics,

where the typical size of the objects of interest is large enough for using statistical methods but too small for neglecting quantum effects due to the wave nature of electrons. Most activities in mesoscopic physics are still performed at low temperatures, where scientifically interesting phenomena manifest themselves fully. In particular, non-classical aspects of electrical conductance have to be taken into account when, for example, the electron wavefunction is confined into two dimensions (2DEG semiconducting heterostructures), one dimension (carbon nanotubes), zero dimension (quantum dots), when the number of electrons is strongly reduced (single-electron transistors), or when the phase of the electron wavefunction is memorised over the full device length resulting in interference phenomena, like Aharonov-Bohm (AB) effect [2, 3].

The AB interference effect, central to this thesis, is observable at low temperatures in mesoscopic rings [4, 5, 6, 7] or in carbon nanotubes [8] because the quantum phase memory of the electron is not randomised during a travel around the whole circumference. A quantum wave associated to such an electron separates into two partial waves at the entrance into the ring and recombines at the exit, leading to a superposed wave. The superposition results in an interference similar to that of optical waves and can be destructive or constructive, depending on the phase difference. Optical waves acquire different phases because of the path-length difference, whereas electron waves moving along fixed paths acquire a phase difference because of a monotically changing magnetic field. The AB effect gives its signature to the magnetoconductance of a mesoscopic ring as periodic oscillations proportional to $\cos(2\pi\phi/\phi_0)$, where ϕ is the magnetic flux through the ring and $\phi_0 = h/e = 4.14{\cdot}10^{-15}$ Tm^2 (h is the Planck's constant and e the electron charge). The same type of electron behaviour is leading to other quantum conductance corrections, i.e. to weak localisation (WL) [9] and to universal conductance fluctuations (UCF) [10]. The former is due to the interference of electron paths with their time-reversed counterparts, and the latter is a consequence of the interference of possible electron paths among themselves. The three above mentioned phenomena have a common origin in the sense that the electron paths are defined by elastic scattering processes. Moreover, UCF and WL can be observed in various mesoscopic geometries, as they

do not depend on a geometry imposed on the electron's paths. WL can easily be detected in macroscopic samples as well.

In this thesis the AB effect in mesoscopic gold rings as well as the UCF in mesoscopic wires are studied. Emphasis is put on the non-equilibrium situation [11], where an interesting enhancement of the coherence phenomena is observed for a large superimposed DC bias voltage ($eV_{DC} \gg k_B T$). As the voltage further increases, the amplitude of the coherence phenomena decreases due to inelastic processes. The voltage dependence of both UCF and AB coherence effects are expected to exhibit a similar behaviour since they both rely on the same principles. However, the constraints imposed by the different geometries affect the decoherence procedures, which is observable in the decay of the phenomenon amplitude for the different UCF and AB effects.

These results show the possibility to study decoherence as a function of the voltage instead of the temperature and are presented in this thesis as the central part of Chapter 5. An outline of the models for describing mesoscopic metallic conductors (Chapter 2) and an overview of the sample-fabrication method (Chapter 3) will precede a description of the measurement setup in Chapter 4. In addition to these chapters, an interesting production method of some other type of mesoscopic samples will be presented in Appendix A. It reports on a very challenging technological work, which was carried out prior to these experiments about coherence effects. Two complementary techniques (EBL and electrochemistry) were combined together to enable electrical studies on special materials, which would otherwise remain unavailable to mesoscopic physicists.

Chapter 2

Electrical transport in metallic mesoscopic conductors

2.1 Classical conductivity

In the presence of an electric field the movement of an electron in a conductor is classically described by

$$\left[\frac{d\mathbf{p}}{dt}\right]_{scattering} = \left[\frac{d\mathbf{p}}{dt}\right]_{field} . \tag{2.1}$$

The rate at which electrons receive momentum from the external field is exactly equal to the rate at which they lose momentum due to scattering forces. By a simple calculation one obtains the classical Drude conductivity

$$\sigma = \frac{ne^2\tau_m}{m} , \tag{2.2}$$

where τ_m is the momentum-relaxation time, n the electron density and m the effective mass. Direct comparison of τ_m and the average time

τ during which an electron travels freely before experiencing an elastic collision is not possible. At low temperatures electrons are scattered less effectively and need more time to fully relax their momenta, which leads to $\tau_m > \tau$ (see Section 2.4.1). However, for simplicity we can use $\tau \approx \tau_m$ and the corresponding mean free path $l = v_F\tau$, where v_F is the Fermi velocity.

Another way to calculate the conductivity is to consider the current as a diffusion of electrons. Due to the concentration gradient, the conductivity is then given by the *Einstein relation*

$$\sigma = e^2 N_F D \,, \tag{2.3}$$

where N_F is the density of states at the Fermi level and D the diffusion constant.

2.2 Quantum conductance

In mesoscopic conductors the classical conductivity gives no adequate description of the electron transport, highly influenced by the quantum nature of electrons. Therefore, at this point it is appropriate to define a quantity which describes the magnitude of various mesoscopic transport phenomena. One might consider a conductor with dimensions smaller than l between two large contact pads. Such conductors, where electrons undergo only collisions with the boundaries, are called *ballistic conductors*. One might also assume that no other event[1] disturbs the electrons on their way through the conductor. In such a case the conductance should be infinite. However, it is found experimentally (see for example [12]) that the conductance of a ballistic conductor reaches a limit. This is a consequence of the interface between the conductor and the pads. Redistribution of the current among the different current-carrying modes, few in the conductor and many in the pads, leads to the resistance. The mismatch in the number of modes arises from the difference in the energy-subband formation, determined by the width in a standard

[1] One of these would be, for example, a quantum interference of electrons.

approach of quantum confinement. The upper limit of the conductance is given by

$$G_c = \frac{2e^2}{h} M \ , \tag{2.4}$$

where M is the number of modes at the Fermi energy. The conductance of one perfect mode without spin degeneracy equals $G_0 = e^2/h = (25.8\ \mathrm{k}\Omega)^{-1}$, a quantity called *quantum conductance*.

2.3 Quantum coherence of electrons

In this section some important transport phenomena are described of which the origin is quantum coherence of electrons. Details of the conditions which have to be fulfilled for the appearance of quantum coherence are given in Section 2.4.2. If not specified differently, the discussion below refers to *diffusive* motion of electrons.

In the Drude model no attention is given to the wave nature of the electrons. Propagation of an electron from a point X to a point Y (Fig. 2.1) includes all possible paths (for simplicity, only two paths are taken into account here) between the scatterers. The transmission probability depends on the phase difference $\Delta\varphi = \varphi_2 - \varphi_1$ acquired by an electron during its travel along the paths 1 and 2:

$$P_{X\to Y} = |A_1 + A_2|^2 = |A_1|^2 + |A_2|^2 + 2|A_1||A_2|\cos(\Delta\varphi) \ , \tag{2.5}$$

where $A_i = |A_i|e^{i\varphi_i}$ are complex amplitudes describing the electron motion. The first two terms on the right-hand side of Eq. (2.5) give the classical Drude conductivity, whereas the last term accounts for the quantum interference.

2.3.1 Weak localisation

The most general interference phenomenon in conductors is the WL. It can be significant even in macroscopic samples and its signature is

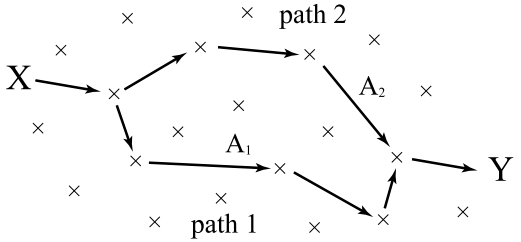

Figure 2.1: Two possible paths from X to Y, with complex transmission amplitudes A_1 and A_2. Elastic scatterers are depicted by crosses.

observable as a decrease of a sample's conductance below the classical value. Due to this interference the correction to the classical conductance is of the order of

$$\Delta G = \langle G_Q \rangle - G_{CL} \sim -\frac{e^2}{h} \, . \tag{2.6}$$

Unlike classical transport phenomena, WL is sensitive to the phase relaxation (characterised by a quantity l_φ, the phase-relaxation length) and not just to momentum relaxation, and it can be probed experimentally by its characteristic magnetoconductance. In particular, for a 1-D sample[2] of a length L the conductance is lowered as

$$\Delta G = \langle G_{WL} \rangle - G_{CL} = -\frac{2e^2}{h} \frac{l_\varphi}{L} \, . \tag{2.7}$$

A phase-coherent conductor can enter another regime called *strong localisation* (SL) if l_φ is of the order or greater than the localisation length $l_c = Ml$, a condition never fulfilled in the present work. In the SL

[2]Defined by both the sample width and thickness being greater than l_φ.

regime a conductor does not show any ohmic behaviour with regard to increasing sample length but an exponential scaling instead [13].

The decrease of the classical conductance is due to an enhancement of the backscattering probability [14, 15, 16]. The probability $P_{X\to Y} = |A_1+A_2+...|^2$ approaches a value $P_{X\to Y} = |A_1|^2+|A_2|^2+...$, because the various trajectories have uncorrelated phases and cancel-out in average. On the other hand the probability $P_{X\to X} = |(A_1 + A_2 + ...) + (A_{1R} + A_{2R} + ...)|^2$ is not influenced by this averaging because A_i and their time-reversed paths A_{iR} are perfectly coherent. This leads to $P_{X\to X} = |A + A_R|^2 = 4|A|^2 = 2P^{no\ coh}_{X\to X}$, where $A = A_R$ in the absence of a magnetic field and $P^{no\ coh}_{X\to X} = |A|^2 + |A_R|^2 = 2|A|^2$. In the presence of a magnetic field the time-reversal invariance is destroyed and the effect disappears.

In materials[3] with strong spin-orbit (SO) interaction the constructive superposition of the propagation amplitude with its time-reversed counterpart is changed in a destructive way [17], which results in an increased conductance. This effect is called *weak anti-localisation* (WAL). In the WL regime, the conductance as a function of the magnetic field is thus positive whereas it is negative in the WAL regime.

2.3.2 Universal conductance fluctuations

Quantum conductance depends on the positions of the scatterers as well, leading to fluctuations which are sample specific. Experimentally, these fluctuations have been observed. For example, by studying the conductance of a sample as a function of a magnetic field [4, 18]. The phase of the electron's wavefunction is sensitive to the vector potential $\mathbf{A}$, and thus a magnetic field changes the phase relationship of the different paths randomly. These fluctuations can also be studied as a function of the Fermi energy [18, 19], which has an effect on the phase as well. In statistical sense, varying the magnetic field or the Fermi energy is equivalent to changing the configuration of the scatterers[4]. The magnitude of these conductance fluctuations is around $\sim e^2/h$ even if the

[3] Those comprising heavy atoms.

[4] Ergodic assumption put forward by Lee and Stone [18].

background conductance varies over several orders of magnitude. Furthermore, at zero temperature the magnitude does not change regardless of the degree of disorder (provided that the transport is diffusive $L \gg l$) and is independent on the average conductance $\langle G \rangle$. For this reason Lee and Stone [18] used the term *universality*, and the phenomenon is called *universal conductance fluctuations* today. More accurately the UCF amplitude is described by $C \cdot \beta^{-1/2} \cdot e^2/h$, where C depends on the dimensionality of the sample and on the spin-orbit interaction (of order unity if $L > w$), and where β accounts for the breaking of time-invariance symmetry at high magnetic field (β =1 is changed in $\beta = 2$ in case of broken symmetry).

At a non-zero temperature the UCF magnitude is reduced below $\delta G_{UCF} = C\beta^{-1/2}e^2/h$. One reason is a finite phase coherence length l_φ, another is the effect of thermal averaging characterised by the thermal length $l_T = \sqrt{\hbar D/k_B T}$. Below is the description of the characteristic UCF regimes in the case of 1-D conditions which are relevant for this work.

- $l_\varphi \ll l_T$ (no thermal averaging):

  The dependence on the sample length ($L > l_\varphi$) is obtained by a simple calculation taking into account that a sample subdivides into L/l_φ "resistors" in series:

$$\delta G_{ap.} = \frac{C_1}{\sqrt{\beta}} \frac{e^2}{h} \left(\frac{l_\varphi}{L} \right)^{3/2} , \tag{2.8}$$

  where C_1 is a constant of order unity. If the temperature is raised, the dimension l_φ of a coherent unit becomes smaller, the number of "resistors" increases and the conductance fluctuations decrease.

- $l_\varphi \gg l_T$ (thermal averaging):

  The energy interval $k_B T$ around the Fermi level, the one available for transport, is subdivided into $N \approx k_B T/E_c$ uncorrelated subintervals, each contributing to the phase coherence within itself. E_c is called *coherence energy* and is given by $E_c = \hbar D/l_\varphi^2$ (for

more detail see Section 2.4.3). With respect to Eq. (2.8) ($L > l_\varphi$), $\delta G_{ap.}$ is reduced further by a factor $N^{-1/2} \approx l_T/l_\varphi$, which results in

$$\delta G_{ap.} = \frac{C_2}{\sqrt{\beta}} \frac{e^2}{h} \frac{l_T l_\varphi^{1/2}}{L^{3/2}} , \tag{2.9}$$

where C_2 is a constant of order unity. In the case $L < l_\varphi$, no subdivision into "series resistors" occurs and the coherence energy becomes $E_c = \hbar D/L^2$. Thus, the only cause of the UCF-amplitude reduction is thermal averaging. With $N^{-1/2} \approx l_T/L$ we obtain

$$\delta G_{ap.} \sim \frac{e^2}{h} \frac{l_T}{L} . \tag{2.10}$$

2.3.3 Aharonov-Bohm effect

As described in Section 2.3.2, magnetoconductance fluctuations in a channel geometry are *aperiodic*, since the interfering paths enclose a continuous range of magnetic-flux values. In contrast, a ring encloses a well-defined magnetic flux $\phi = BS$ threading the corresponding area S, and thus imposes a dominating periodic behaviour

$$G(\phi) = G\left(\phi + i\frac{h}{e}\right) \tag{2.11}$$

of the magnetoconductance, where i is an integer number and h/e the period[5]. Eq. (2.11) expresses the fact that an increment of one flux quantum $\phi_0 = h/e$ through the ring changes the phase difference

$$\Delta\varphi = \frac{e}{\hbar} \oint \mathbf{A} \cdot d\mathbf{s} = 2\pi \frac{\phi}{\phi_0} \tag{2.12}$$

between the trajectories by 2π. The fundamental periodicity ϕ_0 is related to the interference of trajectories that make one half-revolution

[5]This equation applies to the h/e periodicity only. If other harmonics are significant, h/e has to be divided by a corresponding integer.

around the ring, as shown in Fig. 2.2 (a). The first lower harmonic $\phi_0/2 = h/2e$ [20] results from the interference after one full revolution (Fig. 2.2 (b)). There is a fundamental difference between these two periodicities:

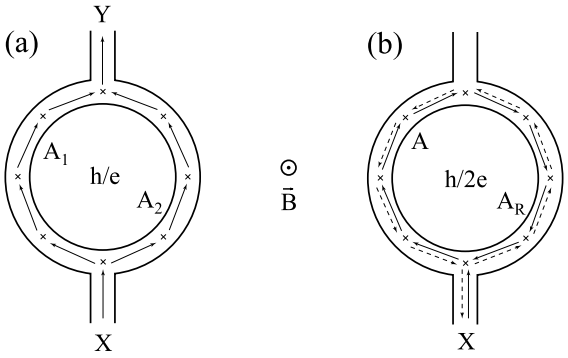

Figure 2.2: (a) h/e oscillations. The electrons encircle one half of the ring. (b) $h/2e$ oscillations. The AB effect occurs because of the interference of time-reversed paths over the whole circumference of the ring.

- The h/e oscillations are dominant in single mesoscopic samples and are sample-specific. The reason for this is that they originate in electron paths which do not interfere with their time-reversed counterparts. Moreover, different configurations of scatterers in different samples influence the aperiodic part of the conductance as well, through the phase factor ϑ in Eq. (2.13). The h/e oscillations, having the same origin as the UCF, are suppressed in macroscopic samples, where many uncorrelated coherent domains of dimension l_φ average out.
- The $h/2e$ oscillations contain a contribution that has a sample-independent phase. A particular path between the scatterers does

not play a role because the interference originates from time-reversed trajectories. The $h/2e$ oscillations can be thought of as a periodic modulation of the WL effect due to coherent backscattering. This effect does not disappear on averaging [20, 21, 22].

Consequently, in a geometry with many rings in series (or in parallel) the h/e oscillations average out [23] whereas the $h/2e$ oscillations remain. However, a strong magnetic field destroys the time-reversal invariance and suppresses the $h/2e$ oscillations, whereas the h/e oscillations remain intact.

In an experiment, both the periodic AB and aperiodic UCF oscillations are observed simultaneously because of the finite arm width of a ring. The aperiodic oscillations lead to a modulation of the oscillation amplitude and phase. Therefore in a ring geometry the magnetoconductance is given by [24]

$$G(B) = \sum_{n=0}^{\infty} r_n(B,\epsilon)\cos\left(2\pi n\frac{\phi}{\phi_0} + \vartheta_n(B,\epsilon)\right) , \qquad (2.13)$$

where n accounts for higher harmonics of the AB effect, r_0 describes the aperiodic fluctuations and ϵ is the energy of electrons relative to the Fermi energy. The field dependencies of r_n and ϑ_n are weak in a ring with a good aspect ratio, for example when the area of the hole is considerably larger than that of the annulus [24]. Namely, the variations of r_n and ϑ_n with B originate from the beats caused by semiclassical trajectories enclosing slightly different areas, and for a ring with the linewidth small in comparison with the diameter they are slow with respect to h/e. Furthermore, in a typical mesoscopic ring the circumference C_r is comparable to l_φ, and the $n = 1$ term dominates, describing the simplest possible passing of an electron through the ring without backscattering which would give rise to the higher harmonics. This is a direct consequence of the length scales involved, as the amplitude of the n-th term in Eq. 2.13 is roughly proportional to $\exp(-nC_r/l_\varphi)$, and for $n \geq 1$ we can write $r_n = r'_n \exp(-nC_r/l_\varphi)$ [13].

For $l_\varphi \approx C_r$, the amplitude r_0 is of the order of $\sim e^2/h$ (see Section 2.3.2) and r'_1 typically (0.4 - 0.8)e^2/h if $k_BT < E_c$ [24] (for more

detail about E_c see Section 2.4.3). In the experiments of Chapter 5 the root mean square (rms) amplitudes of the *differential conductance* $\delta G^{d,AB}_{ap.}$ and $\delta G^{d,AB}_{h/e}$ will refer to the amplitudes $r_0/\sqrt{2}$ and $r_1/\sqrt{2}$, respectively.

2.4 Length and energy scales

As discussed in the previous sections, coherent behaviour of electrons depends on various parameters, such as characteristic lengths and energies. For example, a conductor shows simple ohmic behaviour if its dimensions are larger than the de Broglie wavelength λ, the elastic mean free path l and the phase-relaxation length l_φ. If this is not the case, one must go beyond a classical description.

2.4.1 Relaxation time and elastic mean free path

The dynamics of an electron moving in a crystal is well described by the Schrödinger equation and the properties of crystal periodicity. Topological lattice defects, impurities and lattice vibrations (phonons)introduce a departure from perfect crystallinity, which leads to deviations from the above "ideal" behaviour of electrons. Surrounding electrons are a source of scattering processes as well. The total inverse relaxation time is a sum of inverse relaxation times of all scattering processes, as expressed in the Matthiesen's empirical rule.

In mesoscopic conductors at low temperatures the interesting time scale is the elastic relaxation time. Namely, at these temperatures the scattering processes are mainly elastic, since the energy range available for inelastic processes is small. However, as stated in Section 2.1 the momentum-relaxation time τ_m is more appropriate for describing the conductivity. The relationship between τ_m and τ can be expressed as

$$\frac{1}{\tau_m} \approx \frac{1}{\tau}\alpha_m \,, \tag{2.14}$$

where the factor $0 < \alpha_m < 1$ is related to the effectiveness of an individual collision in destroying the momentum. Without a substantial loss of

generality, at low temperatures we can use τ and the related elastic mean free path $l = v_F\tau$ as the appropriate parameters that enter descriptions of electronic transport in solids.

Because the samples considered in this work are in the diffusive regime ($L > l$), the quantity relevant for describing the electron motion is the diffusion constant

$$D = \frac{1}{d} v_F l \ , \tag{2.15}$$

where d is the sample dimensionality, defined with respect to the length l [25].

2.4.2 Coherence length

The coherence length l_φ mentioned previously is defined as the maximum distance an electron can travel without losing the memory on its phase. The phase-relaxation time τ_φ is related to the coherence length (or phase-relaxation length) by

$$l_\varphi = \sqrt{D\tau_\varphi} \ . \tag{2.16}$$

Quantum corrections to the classical conductance are significant if l_φ exceeds l. In this case a conductor has to be treated as a series of phase coherent units. This condition can be fulfilled at low temperature as far as phase-randomising processes are negligible. Phase-relaxation processes are different from momentum-relaxation processes because the latter do not necessarily lead to randomising the phase of an electron. This can be understood along a motivated discussion in Ref. [13] (although it should be noted that subtle details of l_φ and τ_φ presently attract a considerable amount of attention from scientific committee [26, 27, 28]). Even at this more academic level, one can infer a fundamental distinction between elastic and inelastic processes. Following the Feynman's approach [29], any action which can give information about the path of a quantum interacting particle destroys the interference. Inelastic processes such as scattering on impurities can change the internal degrees of freedom of the impurities, so that it is theoretically possible to obtain

information on electron trajectories by considering the modification of the impurity states. Other examples of phase-randomising sources are collisions with dynamic scatterers (phonons, electrons), magnetic impurities having internal spin states or *ee*-interactions. In contrast, elastic processes are only an implicative source of information.

Even so, these "implications" with l_φ taken in a way phenomenological describe many experimental results astonishingly well, showing that quantum phase of electrons in solids is *a realistic concept and experimentally observable.*

2.4.3 Coherence energy

One might consider an electron confined to a box of size L. In the diffusive regime the time needed to travel the box is given by $\tau_d = L^2/D$. From the Heisenberg's uncertainty relation the related energy level acquires a width

$$E_c = \frac{\hbar}{\tau_d} = \frac{\hbar D}{L^2} \,, \tag{2.17}$$

called *coherence* or *Thouless energy.* The coherence energy in metals is larger than the single-electron energy-level spacing. Thus, a single energy level cannot be considered as being independent, it is correlated with the energy levels lying in the range given by E_c.

If the energy window ΔE contributing to the interference effects[6] is widened up above the value E_c in an experiment, the window is subdivided into $\Delta E/E_c$ uncorrelated energy "bands" of width E_c. Incoherent superposition of these "bands" leads to a weakening of the interference amplitude [5].

Depending on the relevant characteristic lengths E_c changes correspondingly. For example, if the sample size L is larger than l_φ the coherence energy is in a rough picture simply $E_c = \hbar D/l_\varphi^2$. However, in the case of AB interference in a ring the situation is different. The partial waves have to be coherent over the whole circumference in order

[6] ΔE can be due to a finite temperature ($\Delta E = k_B T$) or a bias voltage ($\Delta E = eV_{DC}$)

to show interference so that E_c does not depend on l_φ but on C_r only. E_c for a ring is given by

$$E_c \simeq \frac{\hbar D}{C_r^2} \, . \tag{2.18}$$

Chapter 3

Device fabrication

3.1 Electron-beam lithography

Electron-beam lithography (EBL) is a widely used technique in the field of mesoscopic physics. Structuring methods based on EBL enable engineers to reach submicron dimensions in a very efficient way. Compared to other methods, such as UV- or X-ray lithography, EBL offers an appreciable freedom and flexibility in composing structure patterns, since masks are not required. On the other hand, EBL is less suited for mass production because parallel processing is difficult and the exposure time increases with structure size. EBL is based on writing a pattern in an organic resist layer spun onto a substrate. The resist is sensitive to electrons, for example produced by a scanning electron microscope (SEM), of which the beam deflection can be controlled by a computer and commercial software. Electrons irradiating the resist modify the polymer chains by breaking or cross-linking processes. Thus, illuminated regions can be selectively removed by an appropriate solvent. The created structure serves as a mask for subsequent processes.

A *JEOL JSM-IC848*[1] SEM equipped with a motorised stage, a custom-made beam blanker, an external compensation of environmental magnetic fields and a software of the company *Raith* is used to expose

[1] SEM acceleration voltage of 20 kV.

PMMA[2] or/and the more sensitive PMMA-MA[3] positive resists. The resolution is determined by the spot size of the electron beam, by the forward-scattered electrons, as well as by electrons backscattered by the substrate. This backscattering of electrons causes a supplemental exposure that plays an important role in structural elements lying close to each other (~ 3 μm), which is called the *proximity effect*. Desired undercut in the resist profile (inverted cone, see Fig. 3.1 (b)), which prevents evaporated material on top of the resist from being connected with the one lying on the substrate, is a consequence of the backscattered electrons as well. Small structures are usually fabricated using a positive resist and an additive approach (shown in Fig. 3.1). This method was used in the present work.

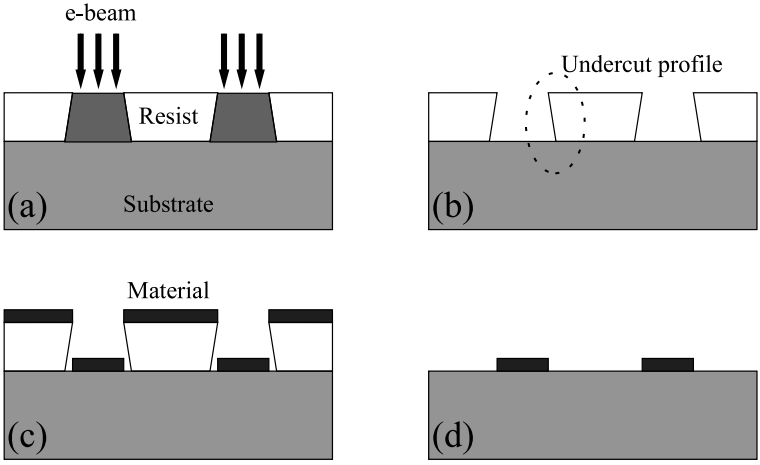

Figure 3.1: EBL using additive pattern transfer and positive resist. (a) E-beam exposure. (b) Development. (c) Evaporation. (d) Lift-off

A focused SEM electron beam cuts polymer chains of a positive resist into small pieces, and cross-links them in a negative one. So, the

[2] **P**oly**M**ethyl **M**eth**A**crylate, *AR-P 671.09 (950 K), Allresist.*
[3] **P**oly**M**ethyl **M**eth**A**crylate co-**M**ethacrylic **A**cid, *AR-P 610.08, Allresist.*

molecular weight is locally modified by the beam. Low-molecular-weight parts can be easily removed by a chemical developer. After the development of a positive resist, the non-exposed regions create the mask. For a negative resist, the mask is composed by the exposed regions. The cutting or cross-linking processes are characterised by the clearance dose, given in charge per unit area, which describes the dose required to fully remove the exposed resists in the development process. In the additive approach the mask is used to transfer a pattern by material evaporation, whereas in the subtractive approach the mask protects the material and the pattern transfer occurs by etching processes. The remaining mask is lifted-off by chemical or physical methods.

3.2 Evaporation of a metal

E-beam evaporation is one of the several methods for depositing a thin layer of a material onto a surface. In particular, it is suitable for depositing metals like Au, Ag, Cu, Ti or Ni, which are relevant for this work. This step, subsequent to EBL in the case of the additive approach, is carried out using a *Balzers PLS 500* evaporation system equipped with an electron gun and its controller (*Telemark* company). The metal to be evaporated is located in a water-cooled copper pocket. If necessary, a graphite liner can be used in order to avoid alloying of the copper part and the metal. Liquefaction of the pocket content is obtained by irradiation using focused[4] energetic electrons produced by an electron gun. The thickness of the evaporated material is measured continuously by a quartz resonator and the evaporation rate is adjusted by the controller. During the evaporation the chamber is cooled by a continuous flow of water. Vacuum in the chamber can be significantly improved by condensating the residual gases by a liquid-nitrogen cooled absorber within the chamber. The best vacuum that can be obtained is of the order of 10^{-9} mbar. Liquid nitrogen is also standardly used for cooling the sample holder down. This prevents excessive heating of the resist by hot metal atoms and thermal radiation of the pocket, which otherwise may result

[4]The focusing is realised using a magnet located nearby.

in unwanted and uncontrolled organic outgassing [30] (such as PMMA sublimation). In addition, the sample holder can be rotated and tilted within a considerable angular range (360° for the rotation and ±40-50° for the tilt).

3.3 Ar sputtering

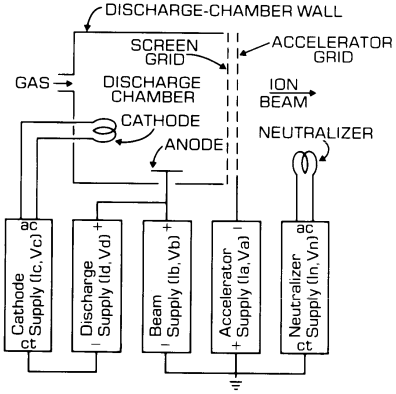

Figure 3.2: Schematics of an Ar sputtering gun.

If required, samples mounted onto the holder of the evaporation system can be sputtered by an in-situ-produced Ar beam. A constant flow of Ar gas is established in the vacuum chamber up to a certain pressure value (typically 10^{-4} mbar). A gas discharge between an anode and a heated cathode locally ionises the Ar atoms. These ions are biased to some energy and directed toward the sample holder. The produced Ar^+ ions are neutralised on their way by an electron spray (thermally emitted electrons). The neutralisation prevents destructive arc discharges generated in the evaporation machine by beams of charged particles. Thus, a neutral and inert flow of Ar atoms etches any material in a pure mechanical way. This method of sample sputtering is very efficient for cleaning

a surface prior to metal evaporation, which is in many cases crucial for obtaining high-quality, stable polycrystalline metallic films.

3.4 Fabrication of gold nanostructures

The substrate used in this work is monocrystalline silicon covered by a thermally grown, 400 nm thick SiO_2 (insulating) layer. Organic particles, often contaminating the substrate surface, must be removed before any subsequent step. Several techniques are used with similar efficiency, such as cleaning processes using mixtures containing acids (H_2SO_4:H_2O_2=3:1) or organic solvents. The cleaning method chosen here consists of cleaning the substrate for several minutes in an ozone oven, followed by sonication in IPA[5] and in ethanol. Once the substrate is clean, a double-layer resist is spun and baked. The bottom layer is 450 nm thick PMMA-MA, and the top one 270 nm thick PMMA. The double-layer technique is often advantageous in the fabrication of a desired structure. It offers a significant tolerance in creating a pronounced undercut profile [31] for our 2 mm large samples (see Figs. 3.6 and 3.8), the EBL exposure of which generally remains unaffected by a badly focussed electron beam due to changes of the writing-field (WF) size and/or a slightly tilted sample. These problems were frequent when a single PMMA layer was used.

Fig. 3.6 and Fig. 3.8 (Section 3.5) show the EBL structure patterns used for the fabrication of the AB and the UCF samples (shown in Figs. 3.3 and 3.4, respectively). The smallest WF (50×50 μm^2) of the EBL step is the most important one because it is used to structure the smallest features of the design. For the AB sample three different exposure steps are performed (Table 3.1), whereas two steps are used for the UCF sample fabrication (Table 3.2). Changing the size of the WF is accompanied by changes of the exposure parameters (beam shift, beam tilt and zoom) which have to be determined by a precise calibration using a special commercially available sample of known dimensions[6]. This

[5] 2-isopropanol.
[6] A fractal-like "chess-field".

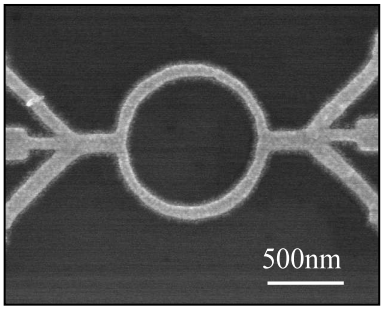

Figure 3.3: AB gold ring (diameter 1 μm, thickness 18 nm, width 90 nm).

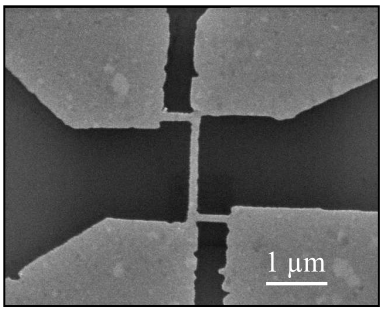

Figure 3.4: UCF gold wire (length 1.5 μm, width 130 nm, thickness 20 nm).

calibration prevents misalignments between different WFs. Corrections of the exposure dose due to the proximity effect are determined empirically. Note that a slightly overexposed dose was deliberately chosen to perform EBL.

Before mounting a sample into the evaporation system, a development is made using a 1:3 mixture of MiBK[7]:IPA for 45 s. A 20 nm thick gold layer is evaporated at a pressure of $1{\cdot}10^{-5}$ mbar (pressure before the evaporation $\sim 1{\cdot}10^{-7}$ mbar). In order to avoid heating the resists, the thermal contact between the sample and its holder[8] is improved using a thermally-conducting paste. Adhesion of the metal to the silicon oxide is improved by in-situ Ar sputtering prior to evaporation (10 s at 4 sccm Ar flow). After the lift-off and cleavage procedures the sample is glued onto a chip carrier and bonded ultrasonically by 50 μm Al wires, thus

[7] 4-**M**ethyl-2-pentanone **iso**-**B**utyl-methyl**K**eton

[8] The holder is cooled by liquid nitrogen, see Section 3.2.

AB sample fab. steps	Writing field size	E-beam current	Step size	Exposure dose
Ring & leads	50 μm	34 pA	20 nm	3 nC/cm 450 μC/cm^2
Leads	200 μm	87 pA	20 nm	550 μC/cm^2
Leads & pads	2 mm	12 nA	200 nm	750 μC/cm^2

Table 3.1: Parameters used for the three successive fabrication steps of the AB samples

UCF sample fab. steps	Writing field size	E-beam current	Step size	Exposure dose
Wires & reservoirs	100 μm	34 pA	20 nm	3 nC/cm 450 μC/cm^2
Leads & pads	2 mm	15 nA	200 nm	750 μC/cm^2

Table 3.2: Parameters used for the two successive fabrication steps of the UCF samples

becoming accessible to external electronics (Fig. 3.5). At this point the chip carrier can be inserted into a socket and the sample is ready to be tested or measured. At any time after evaporation the sample can be observed and visually checked using a SEM (*Philips XL30 FEG*). Once the fabrication process has been completed the sample is stored at liquid nitrogen temperature to prevent clustering of the gold polycrystalline grains.

The samples were produced in one EBL and evaporation step, without using any tilt-angle technique [32] for increasing the thickness of the contact pads. This was done for the following reasons:

- The evaporated gold is pure enough to diffuse on the substrate relatively quickly and to aggregate into clusters. Therefore any resist-baking step following the evaporation inevitably damages the sample and prevents a subsequent EBL.

- A ring is not a geometrical structure suitable for a tilt evapora-

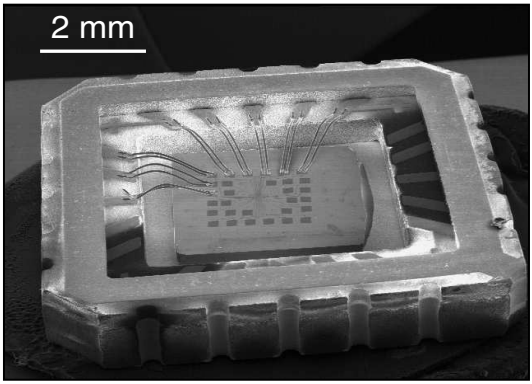

Figure 3.5: Sample glued onto a chip carrier and bonded with Al wires.

tion, unless very high evaporation angles ($\pm$ 45°) are used. The high-angle technique was tested in an attempt to avoid problems in bonding thin structures[9] like those used here. Although the samples were produced with relative success [33], significant lift-off difficulties appeared and this approach was abandoned. Improving the bonding method turned out to be considerably easier.

3.5 Synoptic views

In this section schematic views and SEM photographs of different samples are shown. Three sequential lithographic exposure steps (two only in Fig. 3.8) can be clearly distinguished.

The SEM magnification, writing current and the corresponding exposure parameters are changed after each step. The alignment between different WFs is achieved by a precise calibration procedure (shortly described in Section 3.4), which also requires an accurate adjustment of the SEM column. So, the EBL alignment marks were not necessary. In

[9] Thickness of $\sim$ 20 nm.

practice, more than one device is patterned in a single EBL step. The reason is that mesoscopic samples are rather delicate, and one cannot expect a 100% yield. This is illustrated in Fig. 3.6 and related comments.

Comments to Fig. 3.6 (AB sample):

(a) Contact pads and leads: a (2×2 mm^2) large WF is exposed with a dose of 750 μC/cm^2 and an e-beam current of 12 nA. The steps between successive e-beam movements are 200 nm.

(b) Leads: the WF is (200×200 μm^2) large, the dose 550 μC/cm^2, the current 87 pA and the steps 20 nm.

(c) Rings: the WF is (50×50 μm^2) large. The rings are written as lines with a dose of 3 nC/cm, an e-beam current of 34 pA and a step size of 20 nm. 300 nm away from the rings, the leads are broadened and written as rectangles with a dose of 450 μC/cm^2 (the step size and current remain the same). A series of 5 rings with each 6 leads has been designed in order to reach a high yield.

(d) SEM picture of a ring (width 90 nm, thickness 18 nm, diameter 1 μm). The broadening of the leads can be seen as well.

(e) SEM picture corresponding to (b).

(f) SEM picture corresponding to (a).

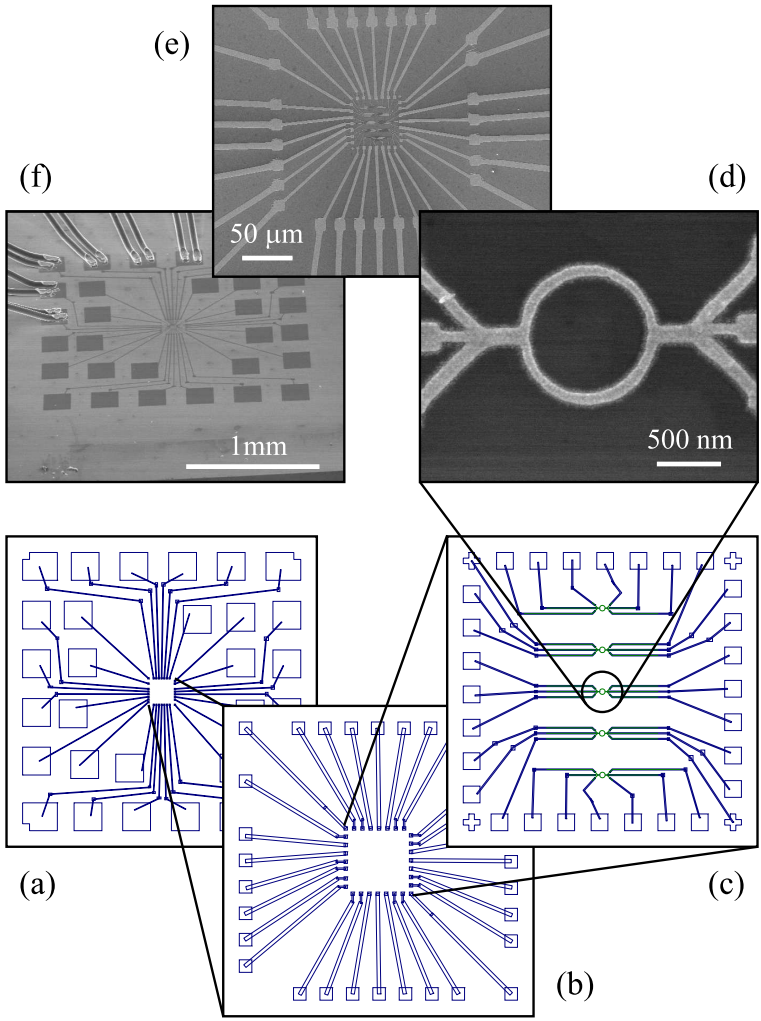

Figure 3.6: AB sample. See designations in text for explanations.

Comments to Fig. 3.7 (special AB sample with heating wire, see Section 5.8):

(a) Contact pads and leads: a (2×2 mm^2) large WF is exposed with a dose of 750 μC/cm^2 and an e-beam current of 12 nA. The steps between successive e-beam movements are 200 nm.

(b) Leads: the WF is (200×200 μm^2) large, the dose 550 μC/cm^2, the current 87 pA and the steps 20 nm.

(c) Rings: the WF is (50×50 μm^2) large. The rings are written as lines with a dose of 3 nC/cm, an e-beam current of 34 pA and a step size of 20 nm. As for the previous synoptic view (Fig. 3.6), the leads are broadened and written as rectangles with a dose of 450 μC/cm^2 (step size and current remain the same). The meander line, connected to the ring by a short wire, is 120 μm long and 400 nm wide.

(d) SEM picture of a ring (width 130 nm, thickness 18 nm, diameter 1 μm).

(e) SEM picture corresponding to (c).

(f) SEM picture corresponding to (a).

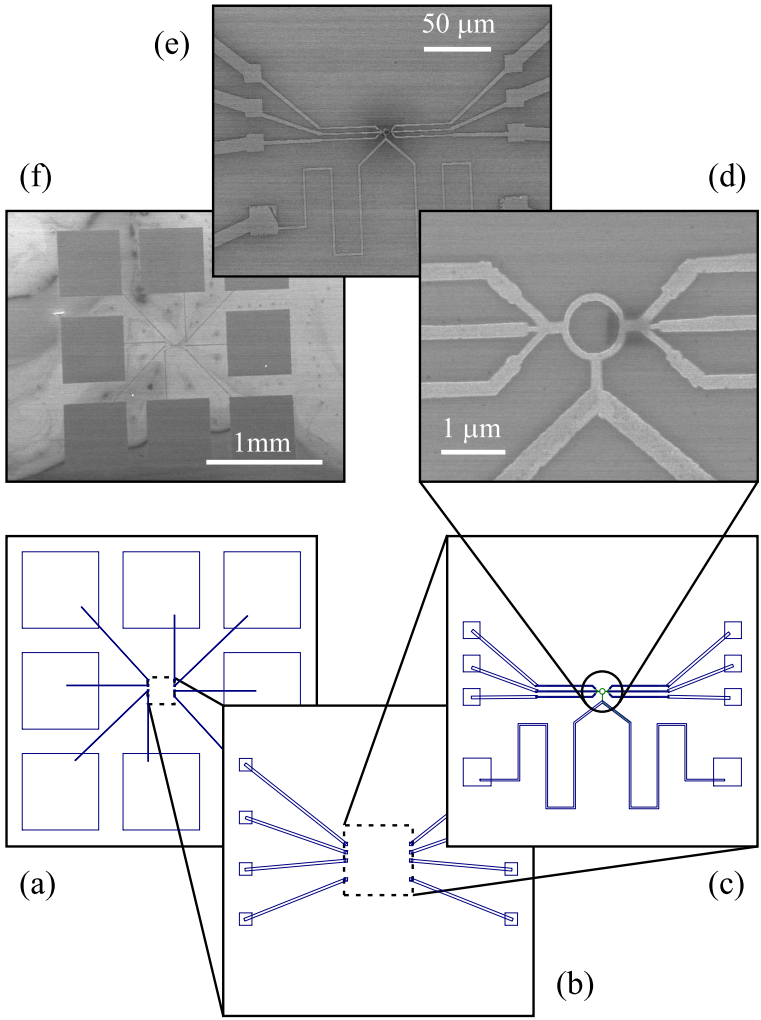

Figure 3.7: Special AB sample with heating wire. See designations in text for explanations.

Comments to Fig. 3.8 (UCF sample):

(a) Contact pads and leads: a (2×2 mm^2) large WF is exposed with a dose of 750 μC/cm^2 and an e-beam current of 15 nA. The steps between successive e-beam movements are 200 nm.

(b) Reservoirs and wires: the WF is (100×100 μm^2) large. The different wires (see point (c)) are written as lines with a dose of 3 nC/cm, an e-beam current of 34 pA and a step size of 20 nm, whereas the reservoirs are written with an area dose of 450 μC/cm^2 (step size and current remain the same).

(c) SEM picture of a wire (width 130 nm, thickness 20 nm, length 1.5 μm).

(d) SEM picture corresponding to (b). Three different wires are patterned. The long one is 170 nm wide, 98 μm long and 20 nm thick and designed for WL measurements, whereas the short ones are 130 nm wide, 1.5 μm long and 20 nm thick and are used to perform UCF measurements.

(e) SEM picture corresponding to (a).

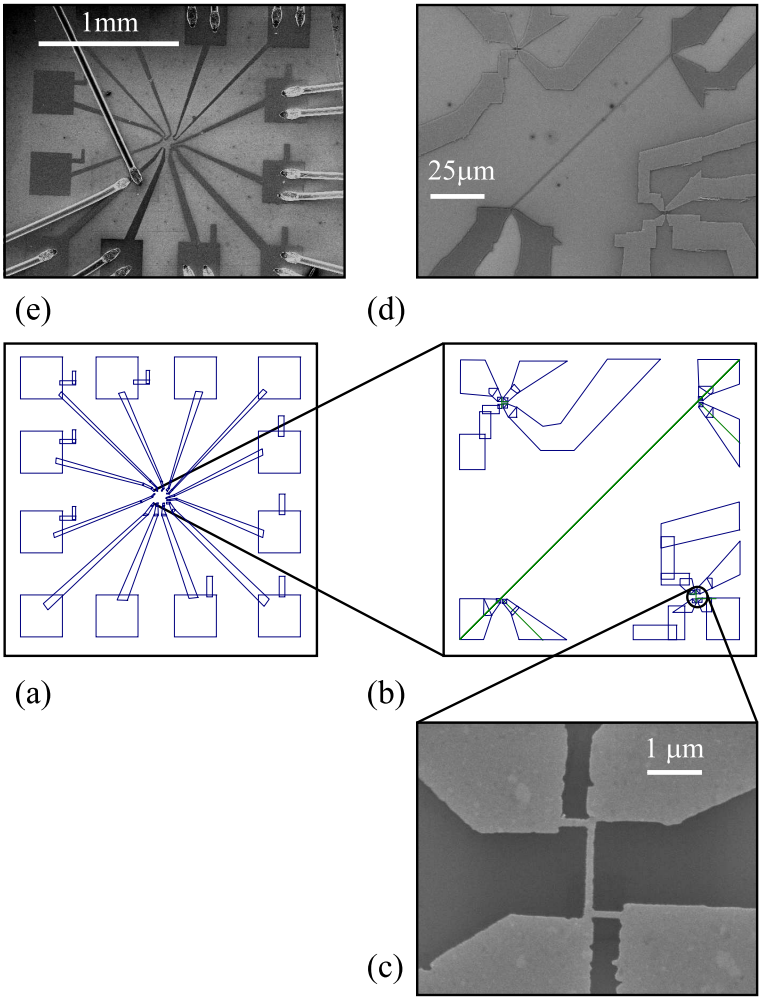

Figure 3.8: UCF sample. See designations in text for explanations.

Chapter 4

Measurement setup

Observation of the AB or UCF effects requires samples which are able to show coherence. To fulfill this condition the typical dimensions of the samples and the coherence length of the electrons have to be of the same order of magnitude ($\sim$ 1 μm). The fabrication technique introduced in Chapter 3 allows for reaching those dimensions easily. In order to reach the desired coherence length l_φ $\sim$1 μm, precautions have to be taken to avoid magnetic impurities which can be phase destructive and therefore the use of pure material is imperative. Low temperatures help to suppress inelastic scattering and thus enhance phase coherence. The relevant energies are of the order of μeV - meV (for example E_c, Table 5.3), energies which correspond to a few K. Thus the measurements are done in a *Cryogenics* ^{3}He cryostat with a base temperature of 270 mK.

4.1 ^{3}He cryostat

In ^{3}He cryostats (see Fig. 4.1) two cooling systems, both relying on adiabatic expansion, are combined. Pre-cooling is achieved by pumping liquid ^{4}He through a needle valve into a small container called a *one-kelvin* pot. By pumping the helium gas away the temperature of the liquid ^{4}He can be lowered down to $\sim$1.4 K. The second cooling sys-

tem consists of a ^{3}He gas container located at room temperature and connected by a long tube to a second container (^{3}He pot) close to the sample holder (see Fig. 4.2). The tube goes through a charcoal adsorption pump and the 1K pot. When the adsorption pump is at a high temperature ($\geq$ 40K) the ^{3}He gas condenses in the ^{3}He pot. Pressure in the ^{3}He system can be adjusted by the temperature of the adsorption pump. The ^{3}He gas pressure depends on the adsorption of ^{3}He atoms on the surface of the cold charcoal. The highest adsorption occurs at low temperatures. As a consequence the ^{3}He liquid is cooled down. The ^{3}He bath is connected to the sample holder via a copper bridge. The thermal coupling of the device to the bath is provided by the bonding wires and thermal radiation. With the ^{3}He completely condensed in the ^{3}He pot, a sample can be kept at 270 mK for 10 - 13 hours. Heating of the sample to higher temperatures is achieved by using a heater close to the sample, which is controlled by a commercial temperature controller. Furthermore, the cryostat is equipped with a superconductive magnet providing a magnetic field of 11 T at 4.2 K.

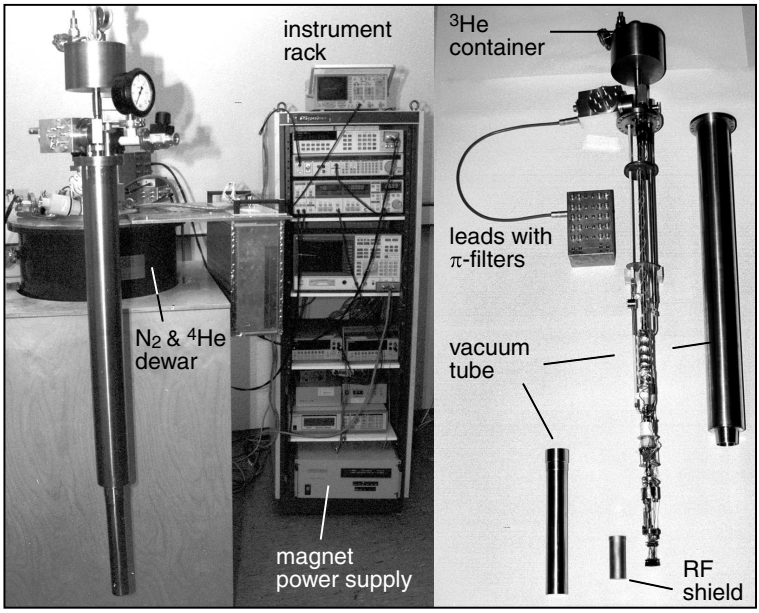

Figure 4.1: Left side: ^{3}He cryostat with the instrument "rack". The insert, normally immersed in liquid helium, is hanging in front of the dewar. Right side: details of the insert when the tube for the isolation vacuum is removed. All the wires are connected to π-filters at the top of the insert.

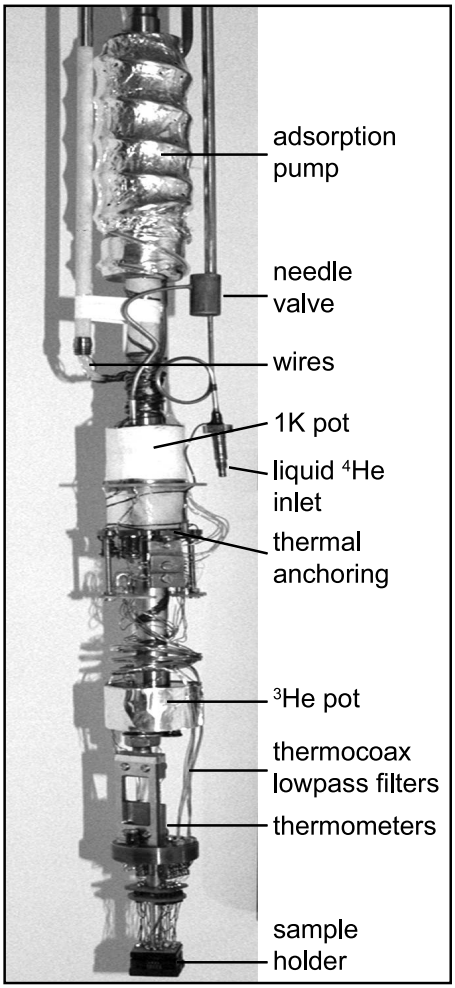

Figure 4.2: Bottom part of the insert.

Higher fields (up to 16 T) can be reached by increasing the critical current of the superconductive coil. This is achieved by pumping away liquid ^{4}He at the λ-plate, which cools down the neighbourhood of the magnet to 2.2 K.

To really reach low sample temperatures an additional effort has to be made. Even when the bath temperature is low the sample temperature can be higher due to RF radiation heating [34]. Therefore the sample stage is equipped with an RF-tight copper box, and all wires leaving the box are "thermocoax" cables from *Philips*. They consist of a wire in a fine stainless steel jacket. The insulation between the wire and the outer shell is made of a mineral powder. The thermal conduction is nearly temperature independent and 20 times smaller than room-temperature conduction of copper. The jacket around the wire has two effects: screening of microwaves and attenuation of high frequency AC currents in the wire itself.

4.2 Measurement technique

The electrical measurements were performed by means of a lock-in amplifier (*SR 830 DSP*) at low frequencies and low excitations[1], using an Adler-Jackson bridge (Fig. 4.3). This method allows compensation of the resistance of a sample at a given temperature and magnetic field by a variable resistor. If the sample resistance R changes, the lock-in measures a voltage proportional to the difference between R and the variable-resistor value R_0, $V_{lock-in} \propto \Delta R = R - R_0$. This technique has the advantage to offer an excellent accuracy in measuring small differences ΔR around a fixed compensation value R_0, independent of the magnitude of R. The signal[2] is amplified by a low-noise preamplifier (108×, *SR 552*) for better accuracy and measured with a typical sensitivity of ≈ 0.3 nV.

Differential resistance measurements as a function of current can be carried out by superimposing an alternating current I_{AC} of a low amplitude to a DC current I_{DC} to the sample, and measuring the AC voltage drop by means of the lock-in. Because the measurement is made using a low amplitude, the result is a good estimate of the differential resistance $dV/dI(I_{DC})$. Together with the Adler-Jackson bridge technique we can accurately determine the fluctuations $\delta[dV/dI] = \delta(\Delta R) = \delta R$ of the sample resistance as a function of a magnetic field and for a given DC current.

The magnetoresistance measurements have been performed by sweeping a magnetic field at a low rate of 0.15 mT/s with an estimated sensitivity of 0.02 mT. The measurements in Chapter 5 are expressed as the magnetoconductance $\delta G^d = \delta[dI/dV] = -(1/R_0^2) \cdot \delta[dV/dI] = -(1/R_0^2) \cdot \delta R$.

[1] $eV_{AC} \lesssim k_B T$.

[2] The off-phase component never exceeds 5 % of the in-phase component.

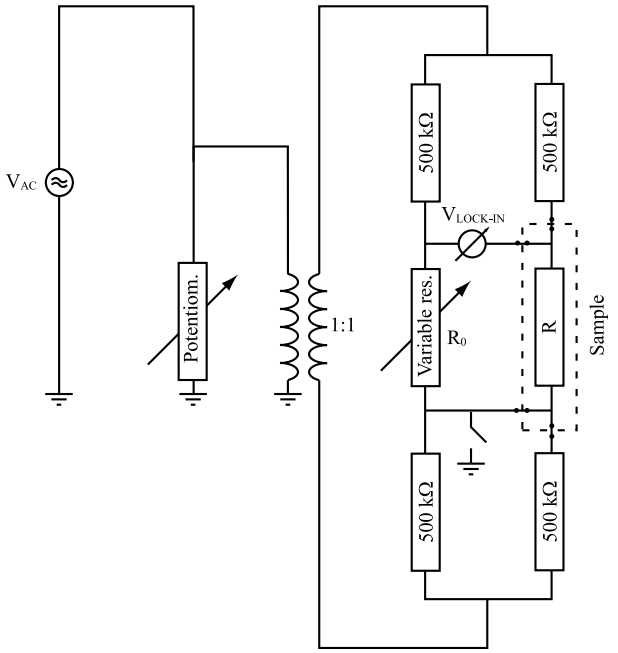

Figure 4.3: Schematic of the Adler-Jackson bridge used for magnetoconductance measurements.

Chapter 5

Non-equilibrium coherence phenomena

Aperiodic fluctuations in electrical conductance of small disordered metallic samples have been studied as a function of magnetic field [4, 18], Fermi energy [18, 19] and configuration of defects [35, 36]. These fluctuations are generally well explained by the theory of UCF (see Section 2.3.2 and [18, 37, 38]). The connection between the above external parameters, all leading to similar conductance fluctuations, was established by an ergodic assumption of Lee and Stone [18]. Conductance fluctuations as a function of an applied voltage [39, 40, 41] have been studied both experimentally and theoretically. For example, Larkin and Khmel'nitskiĭ [11] have found theoretically that in the $V \gg V_c$ regime[1] the rms amplitude of the fluctuations for the differential-conductance G^d is given by

$$\delta G^d_{ap.}(V) \sim (e^2/\hbar)\sqrt{V/V_c}\,, \tag{5.1}$$

Experimental verification of this prediction was however in a way controversial. Namely, Ralph et al. [40] measured a voltage-independent $\delta G^d_{ap.}$ whereas some other experiments [39, 41] showed a certain V-dependence of conductance fluctuations.

[1] See following sections for comments and definitions.

It is unambiguously shown in this work that Eq. 5.1 is *correct* and, moreover, that it can be used as a starting point for explaining the results of similar experiments focused on highly non-equilibrium conditions.

Studies of the *periodic* fluctuations of magnetoconductance were performed for ring geometries (see Section 2.3.3). Since the same coherence mechanism governs the *periodic* and *aperiodic* fluctuations, it is expected to observe some V-dependence of the AB oscillations as well. This has indeed been shown experimentally in [39, 33] and described qualitatively by Häußler [42].

This thesis brings up a study of both the *periodic* and *aperiodic* conductance fluctuations as a function of a large DC voltage as the external parameter and using a magnetic field as the averaging tool [41]. Special emphasis is put on the fluctuations at high DC voltages, where inelastic processes become important and suppress the coherence.

5.1 Equilibrium and non-equilibrium conditions

It is necessary to first outline the expected behaviour of the *aperiodic* fluctuation amplitude with respect to different experimental realisations, *provided that inelastic processes are not important.*

- In equilibrium, $k_BT > eV$, where V is the applied voltage. The range of energies which contribute to the interference pattern is set by k_BT. If k_BT is larger than the coherence energy E_c this energy range subdivides in to $N = k_BT/E_c$ uncorrelated energy intervals. Increase in N results in thermal averaging[2], and a suppression of the fluctuations is expected.

- In out-of-equilibrium conditions, for example if a DC or a low-frequency AC voltage is applied so that $eV_{AC,DC} \gg k_BT$, the energy range leading to ensemble averaging widens up and subdivides into $N = eV_{AC,DC}/E_c$ statistically independent energy in-

[2]See Section 2.3.2.

tervals. With an increase of N, $\delta G_{ap.} = \delta I/V \sim 1/\sqrt{N}$ (because $V \sim N, \delta I \sim \sqrt{N}$) decreases and a damping is also expected.

- An interesting out-of-equilibrium condition is realised by superimposing a large DC voltage $eV_{DC} \gg k_B T$ to a small probing AC voltage $k_B T \gtrsim eV_{AC}$, thus performing a differential measurement $\delta G^d_{ap.}$. In this case an enhancement of the amplitude as a function of the DC voltage is expected instead of a suppression. This enhancement is explained in more detail in Section 5.2.1.

5.2 Non-equilibrium differential conductance

Larkin and Khmel'nitskiĭ [11] calculated the conductance of a small *contact* between two large reservoirs made of normal metals. In particular, they calculated the deviations of this conductance from the ohmic behaviour. An applied voltage across the contact results in a modification of the interference between the partial wavefunctions and affects the conductance. No special attention has been given to the contact geometry, which is considered irrelevant as long as the coherence is possible and its typical size L is larger than the mean free path l (diffusive regime).

5.2.1 Contribution of the quantum interference

Larkin and Khmel'nitskiĭ give a derivation of the fluctuations of the current as a function of an applied voltage. Their result can be understood as follows. At low temperatures ($k_B T \ll E_c, eV_{DC}$) electrons can interfere if their energies are separated by less than E_c. Provided that $V_{DC} \lesssim V_c$ ($V_c = E_c/e$) the current is formed by electrons within the energy range eV_{DC} around the Fermi level. For larger voltages $V_{DC} \gg V_c$ (but still low temperatures, $k_B T \ll eV_{DC}$) the energy range eV_{DC} contributing to the current subdivides into coherent energy intervals of a size E_c, which are uncorrelated among themselves. The number of intervals is given by $N = V_{DC}/V_c$, and each coherent interval contributes randomly

to the quantum correction of the classical current by an amount $(e^2/h)V_c$, a product of e^2/h and the relevant voltage scale V_c. This leads to a total correction to the current $\Delta I_{DC} \sim (e^2/h)V_c \cdot N^{1/2} = (e^2/h)\sqrt{V_{DC}V_c}$.

Fluctuations due to V_{DC} are similar to those caused by a change of the Fermi energy. In both cases the velocities of electrons are influenced, which results in randomisation of the phase given by the interference [41]. Therefore, the current fluctuates around its mean value randomly with an amplitude ΔI_{DC} and a characteristic voltage scale V_c. This can be expressed as $I_{DC} = \langle I \rangle + \Delta I_{DC} \cdot \delta\alpha$, where $\Delta I_{DC} \sim (e^2/h)\sqrt{V_{DC}V_c}$, and $\delta\alpha$ is a random function of V_{DC} which varies with a "frequency" $2\pi/V_c$ ($\delta\alpha = \delta\alpha(V_{DC} \cdot 2\pi/V_c)$) and has the rms amplitude $\langle \delta\alpha^2 \rangle^{1/2}$ equal to 1.

The differential conductance for the above situation is given by

$$G^d = \frac{dI_{DC}}{dV_{DC}} = \frac{d\langle I \rangle}{dV_{DC}} + \frac{d\Delta I_{DC}}{dV_{DC}} \cdot \delta\alpha + \Delta I_{DC} \cdot \frac{d\delta\alpha}{dV_{DC}} \,, \tag{5.2}$$

or equivalently

$$G^d = \langle G \rangle + \left(\frac{d\Delta I_{DC}}{dV_{DC}} + \Delta I_{DC} \cdot \frac{2\pi}{V_c} \right) \delta\alpha \,, \tag{5.3}$$

where the second term on the right hand side represents the fluctuation of the differential conductance:

$$\delta G^d_{ap.} = \delta\alpha \left(\frac{1}{2} \frac{e^2}{h} \sqrt{\frac{V_c}{V_{DC}}} + \frac{e^2}{\hbar} \sqrt{\frac{V_{DC}}{V_c}} \right) \,. \tag{5.4}$$

Since this derivation holds for $V_{DC} \gg V_c$, one finally obtains

$$\delta G^d_{ap.} \propto \frac{e^2}{\hbar} \sqrt{\frac{V_{DC}}{V_c}} \,, \tag{5.5}$$

which anticipates a non-linear enhancement of the fluctuation amplitude of the differential conductance with increasing V_{DC}. The validity of Eq. 5.5 is clearly shown experimentally in Sections 5.4 - 5.5.

In carrying out a differential conductance measurement by simply sweeping the DC voltage, problems in extracting the average fluctuation

amplitude $\delta G^d_{ap.}(V_{DC})$ occur [42] due to sample-specific configuration of scatterers. In this case $\delta G^d_{ap.}(V_{DC})$ can be determined by averaging over a small voltage interval around V_{DC}. Another possibility - exclusively used in the following sections - is to average over a different ensemble at a field V_{DC}, for example to average over a magnetoconductance trace. It was shown experimentally [41] that these two ways of extracting $\delta G^d_{ap.}$ give the same result.

So far no assumption has been made with regard to the ratio L/l_φ, and the above derivation is valid implicitly for $l_\varphi > L$. However, it is expected that inelastic processes (not taken into account until now) alter this behaviour. At high energies electron-electron and electron-phonon interactions give rise to inelastic processes and therefore to a loss of the coherent interference.

5.2.2 Inelastic processes

At high voltages or temperatures inelastic processes which have been ignored so far are significant. These processes can be characterised by the length $l_{in} = \sqrt{D\tau_{in}}$. If l_{in}, which now determines the characteristic energy scale of the coherence, decreases beyond the length L of a sample, the model of Section 5.2.1 is affected.

At $l_\varphi < L$, a division into series "resistors" of length l_{in} occurs. In a single resistor electrons are coherent within the energy interval $eV_c^{in} = \hbar D/l_{in}^2 = V_c(L/l_{in})^2$. The reasoning of Section 5.2.1 is still valid if the voltage drop $V_{in} = V_{DC} \cdot (l_{in}/L)$ over a segment of a length l_{in} is larger than V_c^{in}. Now the energy range eV_{in} subdivides into energy intervals of a size eV_c^{in} and the quantum correction of the current through a resistor is $\Delta I_{in} \sim (e^2/h)\sqrt{V_{in}V_c^{in}}$. Calculation of Section 5.2.1 still holds for a single resistor, and similarly to Eq. 5.5 the fluctuation amplitude of the differential conductance is $\delta G^d_{in,ap.} \propto (e^2/\hbar)\sqrt{V_{in}/V_c^{in}}$. In order to obtain the fluctuation amplitude over the whole length L of a sample, one has to average the *partial* amplitudes incoherently, which results in $\delta G^d_{ap.} = \delta G^d_{in,ap.} \cdot N^{-1/2}$ (where $N = L/l_{in}$). So, in the presence of

inelastic processes the differential-conductance amplitude is given by

$$\begin{aligned} \delta G^{d}_{ap.} &\propto \frac{e^2}{\hbar}\sqrt{\frac{V_{in}}{V_c^{in}}}\cdot\left(\frac{l_{in}}{L}\right)^{1/2} = \frac{e^2}{\hbar}\sqrt{V_{DC}\frac{l_{in}}{L}\cdot\frac{1}{V_c}\frac{l_{in}^2}{L^2}\cdot\frac{l_{in}}{L}} \\ &\propto \frac{e^2}{\hbar}\sqrt{\frac{V_{DC}}{V_c}}\cdot\left(\frac{l_{in}}{L}\right)^{2}, \end{aligned} \tag{5.6}$$

valid for $V_{in} > V_c^{in}$ and $eV_{in} > k_BT$. Expressing them differently, Eq. 5.6 is valid for

$$eV_{DC} > k_BT\cdot\left(\frac{L}{l_{in}}\right) \qquad \text{and} \qquad V_{DC} > V_c\cdot\left(\frac{L}{l_{in}}\right)^{3}, \tag{5.7}$$

which is always fulfilled in the experiments presented in the following sections. Eq. 5.6 shows that the enhancement of the rms amplitude of the differential-conductance fluctuations described in Section 5.2.1 is suppressed at high voltages as a power law.

5.2.3 Periodic fluctuations

The underlying mechanism of the interference phenomenon leading to the fluctuations of differential conductance is universal and applies to any geometry. For a ring, in addition to the *aperiodic* fluctuations, interference imposed by the geometry gives rise to the *periodic* oscillations. If the circumference of the ring C_r is shorter than l_φ or l_{in}, the discussion given in Section 5.2.1 applies to the AB oscillations as well, and their enhancement following Eq. 5.5 is expected. This effect is observed experimentally [33, 42]. In contrast, for $C_r > l_{in}$ the picture of subdivision of a ring into coherent "resistors" in series is not correct, and the functional form of the suppression given by Eq. 5.6 does not hold for the AB oscillations. Namely, only those electrons which remain coherent over the whole length of the loop contribute to the h/e oscillations. In this case the number of electrons of which the phase is not randomised by inelastic processes is reduced exponentially as $\exp(-C_r/l_{in})$. This exponential decay is predicted by an intuitive argument of Al'tshuler and

was experimentally demonstrated in [43] for an Sb ring in equilibrium conditions and for $l_{in} \approx l_\varphi(T)$ inferred from the WAL measurements.

According to [44], E_c for the AB oscillations in a ring is, interestingly, not given by Eq. 2.18, but by

$$E_c^{in} \simeq \frac{\hbar D}{l_{in} \cdot C_r} \ . \tag{5.8}$$

This expression is calculated from the probability $p(t)$ that a carrier interferes with itself at a time t after one passage around the ring, which is a product of the probability that it has diffused all the way around, times the probability that it has not been inelastically scattered:

$$p(t) = \exp\left(\frac{-C_r^2}{Dt}\right) \cdot \exp\left(\frac{-t}{\tau_{in}}\right) = \exp\left[-\left(\frac{C_r^2}{Dt} + \frac{Dt}{l_{in}^2}\right)\right] \ . \tag{5.9}$$

The minimum $t_{min} = l_{in}C_r/D$ of the exponent in Eq. 5.9 determines the maximum of the probability $p(t)$ and is the flight time of importance for determining E_c^{in} (Eq. 5.8). A more accurate calculation shows that E_c^{in} has the precise form

$$E_c^{in} = \frac{\hbar D}{l_{in}^\gamma \cdot C_r^{2-\gamma}} \ , \tag{5.10}$$

with $\gamma = 1.3$ [44].

With the above arguments the voltage dependence of the differential conductance for the AB oscillations in the limit $C_r > l_{in}$ can be obtained as

$$\begin{aligned} \delta G_{h/e}^d &\propto \frac{e^2}{\hbar}\sqrt{\frac{eV_{DC}}{E_c^{in}}} \cdot \exp\left(-\eta \cdot \frac{C_r}{l_{in}}\right) \\ &\propto \frac{e^2}{\hbar}\sqrt{\frac{V_{DC}}{V_c}} \cdot \left(\frac{l_{in}}{C_r}\right)^{\gamma/2} \cdot \exp\left(-\eta \cdot \frac{C_r}{l_{in}}\right) \ . \end{aligned} \tag{5.11}$$

where η is of order 1 and accounts for the deviations in the regime where $l_{in} \ll C_r$ is not satisfied[3] [44]. This expression states that the decay of

[3] The exponential decay is fully developed at $l_{in} \ll C_r$.

the fluctuation amplitude in the differential conductance is steeper than for the UCF. In Section 5.5 it will be shown experimentally that it is indeed the case.

5.3 Equilibrium coherence parameters

In order to discuss the non-equilibrium phenomena it is important to start from the coherence parameters in equilibrium. In general, the loss of coherence can be caused by the electron-electron, electron-phonon and magnetic interactions [45]. Under certain conditions the dephasing occurs in the absence of inelastic processes [46], but elastic scattering at non-magnetic impurities are known to cause no phase randomisation [47]. By fitting the WL theory to the measured change in the resistance as a function of a magnetic field at its low values it is possible to determine the phase coherence time and, consequently, the corresponding length. Theoretically, the phase-breaking rate decreases with temperature as a power law, $\tau_\varphi \propto 1/T^p$, where p varies between 0.5 and 3, depending on the type of interactions and the effective dimensionality of the system.

In the case of a long 1-D wire ($L \gg l_\varphi, w, t$) the WL correction of Eq. 2.7 can be rewritten [48] as

$$\Delta G = -\frac{2e^2}{h}\frac{l_\varphi}{L} \Longleftrightarrow \frac{\Delta R}{R} = \frac{R_\square}{\pi\hbar/e^2}\frac{l_\varphi}{w} \,, \tag{5.12}$$

where $R_\square$ is the sheet resistance and w the width of the wire. The effect of a magnetic field is described by introducing a field-dependent $l_\varphi(B)$ [49]

$$\frac{1}{l_\varphi^2(B)} = \frac{1}{l_\varphi^2} + \frac{1}{3}\left[\frac{\pi w B}{h/2e}\right]^2 \,. \tag{5.13}$$

For a strong spin-orbit coupling the WL correction breaks up into a singlet and a triplet part [17]

$$\frac{\Delta R}{R} = \frac{1}{2}\left(\frac{R_\square}{\pi\hbar/e^2}\frac{l_\varphi(B)}{w}\right) - \frac{2}{3}\left(\frac{R_\square}{\pi\hbar/e^2}\frac{l'(B)}{w}\right) \,, \tag{5.14}$$

where $l'(B)$ is a function of $l_\varphi(B)$ and the spin-orbit scattering length l_{SO}. Therefore, including the spin-orbit scattering accounts for the WL and WAL events:

$$l'^{-2}(B) = l_\varphi^{-2}(B) + \frac{4}{3} l_{SO}^{-2} \, . \tag{5.15}$$

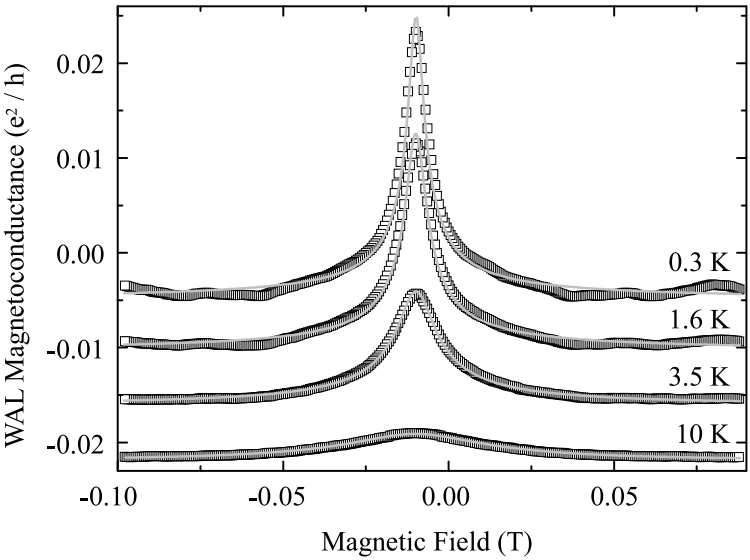

Figure 5.1: WAL curves of a gold wire (length 98 μm, width 170 nm, thickness 20 nm) for four different temperatures. The curves are offset for clarity.

Eq. 5.16 summarises the above effects in an equation comprising l_{SO} and l_φ as fitting parameters.

$$\frac{\Delta G}{e^2/h} = \frac{1}{L} \frac{1}{\sqrt{l_\varphi^{-2} + \frac{1}{3}\left(\frac{\pi w B}{h/2e}\right)^2}} - \frac{3}{L} \frac{1}{\sqrt{l_\varphi^{-2} + \frac{4}{3} l_{SO}^{-2} + \frac{1}{3}\left(\frac{\pi w B}{h/2e}\right)^2}} \, . \tag{5.16}$$

WL measurements have been performed on both AB and UCF gold samples. Gold is known to show strong spin-orbit scattering, and WAL is expected and observed (Fig. 5.1). In addition to the UCF sample (Fig. 3.8), a longer wire has been simultaneously produced on the same chip in order to carry out the measurements of conductance fluctuations and WL on samples of identical material quality. Because of the difference in the amplitudes of WL and UCF with regard to the ratio (l_φ/L), i.e.

$$\text{(UCF)} \quad \delta G_{ap.} \propto \frac{e^2}{h}\left(\frac{l_\varphi}{L}\right)^{3/2}, \quad \text{(WL)} \quad \Delta G = -\frac{2e^2}{h}\frac{l_\varphi}{L}, \qquad (5.17)$$

the WL can be more successfully measured in a long wire ($L \gg l_\varphi$). By this approach the l_{SO} and l_φ can be determined precisely, as shown in Fig. 5.2 (a) and Table 5.1. Reliable determination of l_{SO} is possible at $T = 10$ K, where the magnetoconductance changes its slope at a high field (not shown in Fig. 5.1). Thus determined l_{SO} is used in the calculations for lower temperatures. Unfortunately, in the case of the AB sample no similar wires suitable for the WL measurements have been produced on the same substrate (Fig. 3.6). However, WL has been measured in rings as well and a rough estimate of l_φ has been made (shown in Table 5.1 and Fig. 5.2 (b)). Because the conditions of the evaporation of gold for both AB and UCF samples are very similar (identical pressure, evaporation rate, source of gold) the values of l_φ for the AB sample, lower than the UCF sample values, can be considered as the lower limits.

Since the diffusion constants of the samples differ negligibly (Table 5.2), the result for l_φ obtained by the WAL measurements on the long wire is considered to be the most accurate value. This assumption is justified further by the results of analysis in Section 5.6. Therein it is shown that $l_\varphi(V_{DC} = 0) > l_{Th}$, where l_{Th} is a length which determines the equilibrium coherence energy by geometrical arguments, results in a remarkably consistent picture of the decoherence due to inelastic processes in our samples.

Fig. 5.2 shows the temperature dependence of τ_φ which is qualitatively in agreement with the fact that the mechanism of phase breaking

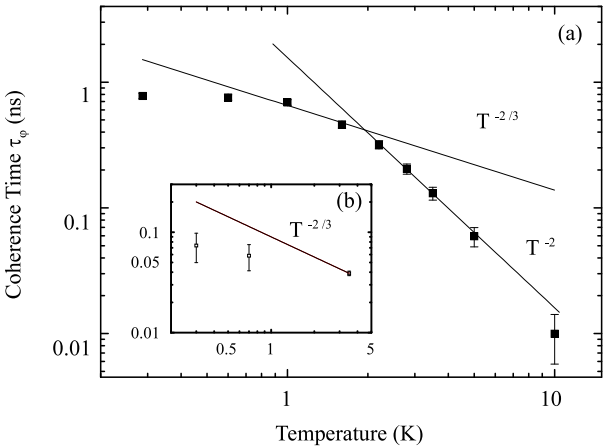

Figure 5.2: Coherence times deduced from WAL measurements, (a) of a 98 μm long gold wire, (b) of a ∅ 1 μm large gold ring.

is dominated by electron-phonon scattering at temperatures above a few K ($\tau_\varphi \propto T^{-2}$) and electron-electron interaction at low temperatures ($\tau_\varphi \propto T^{-2/3}$). A discussion about those slope values is held in Section 5.6. The experiments show a saturation of τ_φ at low temperatures as well, which was observed in other gold samples [26]. The question of the saturation of τ_φ is still a controversial topic which is outside the scope of this thesis.

Finally, Table 5.2 shows the values of the parameters which characterise both the AB and UCF samples. The diffusion constant D is deduced from R_0 and the sample dimensions using Eq. 2.3 (Einstein relation).

Sample	L [μm]	w [nm]	t [nm]	T [K]	l_φ [μm]	τ_φ [ns]	l_{SO} [nm]
UCF	98	170	20	0.3	3.0	0.8	48
(for WL)				3.5	1.2	0.1	48
AB	$\varnothing$ 1	90	18	0.3	$\gtrsim 0.9$	0.07	~ 90
				3.5	$\gtrsim 0.65$	0.04	~ 90

Table 5.1: Coherence lengths and spin-orbit scattering lengths extracted from WAL measurements.

Sample	R_0 (300 K)	R_0 (0.3 K)	$R_\square$	D
UCF	31.9 Ω	18.5 Ω	1.6 Ω	116 cm^2/s
AB	43.0 Ω	25.9 Ω	1.9 Ω	110 cm^2/s

Table 5.2: 4 terminal characterisation at B=0.

5.4 Non-equilibrium universal conductance fluctuations

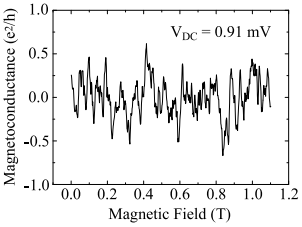

Figure 5.3: Typical UCF magnetoconductance trace at T=0.3 K and V_{DC}=0.91 mV.

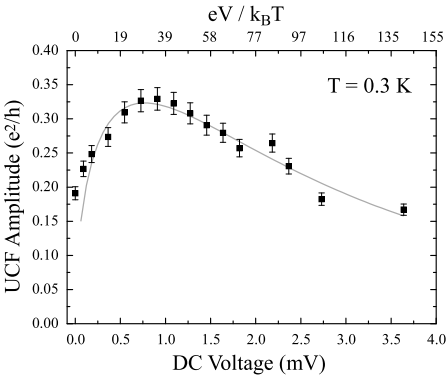

Figure 5.4: UCF amplitude as a function of the superimposed DC bias voltage at T=0.3 K, the line serves as a guide for the eye.

The UCF measurements have been carried out at 300 mK in a ^{3}He cryostat. A DC current I_{DC} (up to 200 μA) resulting in a DC bias voltage $V_{DC} = I_{DC}R_0$ has been superimposed to a small AC current of 1 μA. The energy scales obtained by this approach are summarised in Table 5.3. The magnetoconductance traces have been measured in the field range 0-7 T with a sweeping rate of 0.5 mT/s and a sampling rate of 3 s, which represents a measurement time of $\sim$ 4 hours per trace. Such a typical trace is shown in Fig. 5.3. The reproducibility of the traces (shown in Fig. 5.5) has been checked and remains perfect even after thermal cycling up to several degrees kelvin.

The averaging range of the UCF has been chosen for magnetic field values lying between 5-7 T. It comprises $\sim$ 100 times the correlation field $B_c \approx \phi_0/wL$ = 20 mT. The ensemble averaging over a magnetic

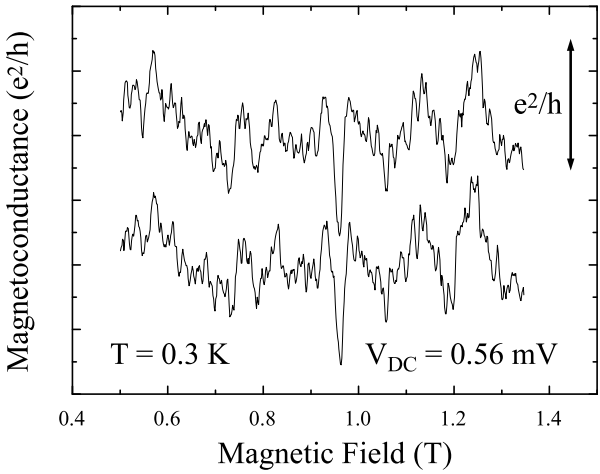

Figure 5.5: Two magnetoconductance traces at $T = 0.3$ K and $V_{DC} = 0.56$ mV as a test of reproducibility. The curves are offset for clarity.

field reduces sample-specific fluctuations and allows to determine the behaviour of the UCF amplitude as a function of V_{DC} independent of the configuration of defects. The rms amplitude of the UCF is given by the standard deviation $\delta G_{ap.}^{d,UCF} = \langle (G^{d,UCF} - \langle G^{d,UCF} \rangle)^2 \rangle^{1/2}$ of the averaging range after having subtracted the coarse background. The superscript *UCF* refers to the wire sample whereas *AB* is related to the ring sample.

At $V_{DC} = 0$, $\delta G_{ap.}^{d,UCF} = 0.19 \cdot e^2/h$, which is smaller than expected. As stated in Section 2.3.2, a UCF amplitude reduction can occur because of the thermal averaging. This is the case in our experiment, since $k_B T$ is larger than V_c for $V_{DC} = 0$. In addition, the time-invariance symmetry is broken at high magnetic field, which leads to a further reduction by a factor of $\beta^{-1/2} = 1/\sqrt{2}$. Thus, a suppression factor of $\beta^{-1/2} \cdot C \cdot l_T/L = 0.24 \cdot C$ is to be taken into account, where C is of order unity.

The UCF amplitude as a function of a superimposed DC voltage is

shown in Fig. 5.4. The amplitude of the UCF increases up to a value of approximately 1 mV, saturates and then decreases. The decay has been measured up to 3.6 mV, which is higher than 40 K if expressed as temperature. According to the theory of Larkin and Khmel'nitskiĭ the increase of the UCF up to 1 mV is expected to behave as a square root. However, it is found that $\delta G_{ap.}^{d,UCF} \propto V_{DC}^{\alpha}$ with $\alpha \sim 0.2$, which is less steep. Experimentally the UCF amplitude is not zero at V_{DC}=0 and therefore an asymptotic behaviour towards the square root is observed, which inevitably reduces the value of α. In addition, a fraction of electrons may already be affected by inelastic processes even at low V_{DC} which can also be a cause for the smaller value of α.

Sample	Oscillation type	E_c [μeV]	eV_{AC} [μeV]	k_BT [μeV]	eV_{DC} [meV]
UCF	aperiodic	3.4	18.5	25.9	0 - 3.7
AB	periodic h/e	0.7	25.9	25.9	0 - 3.2
	aperiodic	1.5	25.9	25.9	0 - 3.2

Table 5.3: Energy scales for the AB and UCF experiments.

5.5 Non-equilibrium Aharonov-Bohm effect

The same type of measurements as for the UCF have been carried out for the AB effect at 300 mK. A DC current (up to 125 μA) has been superimposed to an AC current of 1 μA (the energy scales are summarised in Table 5.3). A magnetic field was swept at a typical rate of 0.15 mT/s and a sampling rate of 1 s. The magnetoconductance traces have been measured from 0 to 2.5 T, representing a measurement time of $\sim$ 5 hours per trace. A single trace (shown in Fig. 5.8) corresponds to approximately $\sim$ 500 AB oscillation periods of $\sim$ 5.1 mT (taken from the peak value of the Fourier spectrum in Fig. 5.7) which is in very good agreement with the sample dimension.

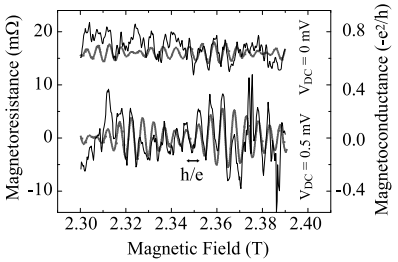

Figure 5.6: Upper curves: part of a magnetoconductance trace (light line) and its corresponding filtered curve (black curve). Bottom curves: similar traces as the upper ones in the presence of a non-zero DC voltage.

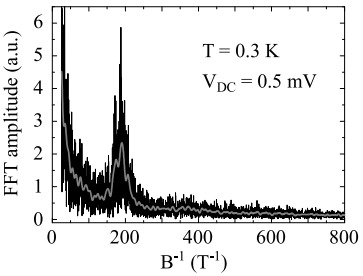

Figure 5.7: Fourier transform of an AB magnetoconductance trace at 300 mK and $V_{DC} = 0.5$ mV, the peak corresponds to oscillations of ~ 5.1 mT period.

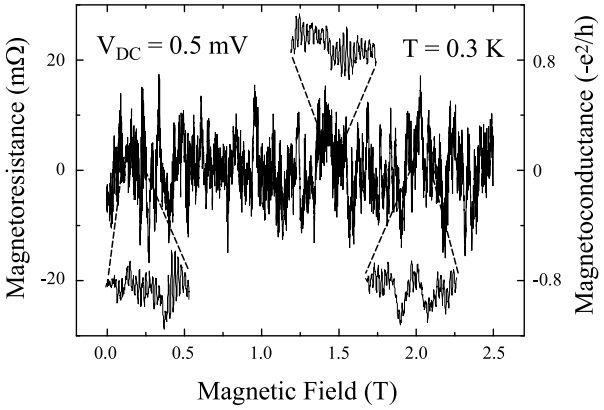

Figure 5.8: AB magnetoresistance trace showing hundreds of periodic oscillations, which are obtained by sweeping the magnetic field for ~ 5 hours.

Because of the finite width ($w \approx 90$ nm) of the AB ring the amplitude of the oscillations does not remain constant and shows beating features (Fig. 5.6) due to the semiclassical trajectories enclosing slightly different areas. For the same reason the UCF is also superimposed and gives rise mainly to the low frequency part in the Fourier spectrum.

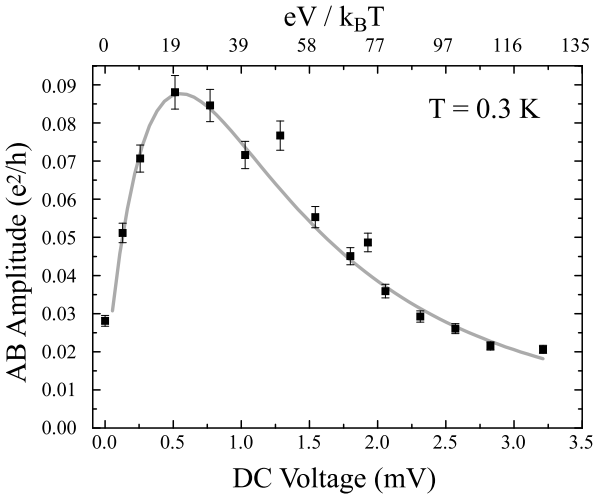

Figure 5.9: AB amplitude as a function of the superimposed DC bias voltage at T=0.3 K, the line serves as a guide for the eye.

The effect of the increase of the oscillation amplitude with increasing V_{DC} is shown in Fig. 5.6. Extracting the average AB amplitude from the whole magnetoconductance trace has been a difficult task because of the finite width of the peak in the Fourier spectrum. Using a digital filter, the aperiodic fluctuations have been subtracted from the magnetoconductance traces and the oscillations smoothed (Fig. 5.6). The rms AB amplitude has been determined by numerical integration.

At $V_{DC} = 0$, the AB amplitude is equal to $\delta G^{d,AB}_{h/e}(V_{DC} = 0) \sim 0.03 \cdot e^2/h$, not (0.4 - 0.8) $\cdot e^2/h$ as expected from [24, 50]. However, this expectation is valid for temperatures $k_B T < E_c$, which is not the

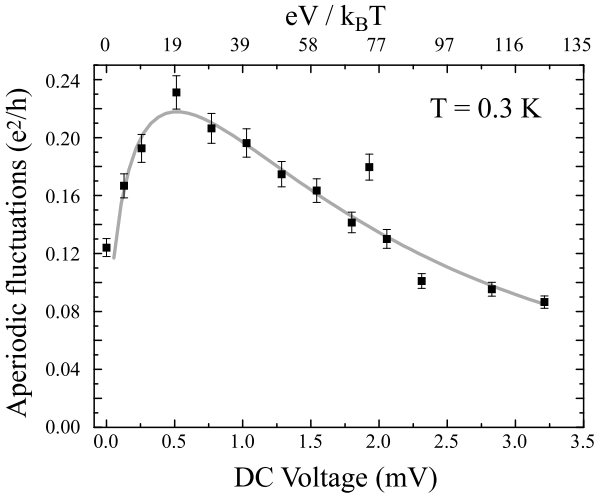

Figure 5.10: Aperiodic fluctuations amplitude extracted from the AB traces as a function of the superimposed DC bias voltage at T=0.3 K, the line serves as a guide for the eye.

case in the experiment for $V_{DC} = 0$ (see Table 5.3). The *aperiodic* fluctuations (see Fig. 5.8) which are superimposed to the AB oscillations can be extracted from a measurement trace as well. At $V_{DC} = 0$ the aperiodic fluctuation amplitude is of order $\delta G_{ap.}^{d,AB}(V_{DC} = 0) \sim 0.12 \cdot e^2/h$, again smaller than unity as in the non-equilibrium UCF measurement. The reduction of this factor from unity can be explained by the thermal averaging, breaking of the time-invariance symmetry and in addition subdivision into series resistors (Section 2.3.2), which leads to an amplitude $\beta^{-1/2} \cdot C \cdot (l_T/l_\varphi) \cdot (l_\varphi/L)^{3/2} \approx (0.04 - 0.10) \cdot C$, where C is of order unity.

The AB amplitude as a function of V_{DC} is shown in Fig. 5.9. The dependence is qualitatively the same as that observed for the UCF amplitude. Namely, an increase of the AB amplitude up to a value of 0.5 mV, a saturation and a decay which has been measured up to 3.4 mV.

Similar to the UCF result, the increase of up to 0.5 mV does not exactly behave as a square root, but as $\delta G_{h/e}^{d,AB} \propto V_{DC}^{0.4}$. This discrepancy can be explained using the same arguments as for the UCF case (see Section 5.4). The steeper decay of the AB amplitude in comparison to the UCF amplitude shows a different functional form of the decoherence, as explained in Section 5.2.3.

The aperiodic fluctuation amplitude $\delta G_{ap.}^{d,AB}$ has been extracted from the AB magnetoconductance trace not only for $V_{DC} = 0$ (as stated above), but for all V_{DC} traces. Fig. 5.10 shows the behaviour of the aperiodic fluctuations found from the AB traces. Similar to the AB amplitude, the saturation of the aperiodic fluctuations amplitude occurs at $V_{DC} = 0.5$ mV. On the other hand, the decay is clearly less steep than the AB decay of Fig. 5.9.

5.6 Discussion

In this section we will discuss the extraction of l_{in} from the above measurements and its voltage dependence. Due to large electric fields applied across the samples and the reservoir which are not massive, one has doubts about the fact that electronic heating affects the effective temperature of the electrons [32, 31, 51, 52]. However, this temperature increase, which is estimated to be as high as $T_e = 5$-12 K according to Eq. 5.20, is still small in comparison to eV_{DC} for all the points except perhaps to one or two at the lowest V_{DC}. For that reason we can neglect the thermal averaging and, analogously to Eq. 5.6, use the expression

$$\delta G_{ap.}^{d,UCF}(V_{DC}) = A_{ap.}^{UCF} \cdot \sqrt{\frac{V_{DC}}{V_c}} \cdot \left(\frac{l_{in}(V_{DC})}{L}\right)^2 . \qquad (5.18)$$

The parameter $A_{ap.}^{UCF}$ is deduced from the first $V_{DC} \gg V_c$ experimental point[4] of Fig. 5.4, assuming that $l_{in}/L > 1$ plays no role[5] and thus setting $l_{in}/L = 1$. Since V_c and L are known, $l_{in}(V_{DC})$ can easily be

[4] In our measurements, it corresponds always to the first $V_{DC} \neq 0$ point.
[5] $l_{in}(V_{DC} = 0) \approx l_\varphi(T = 0.3K)$ leading to $l_{in}/L > 1$ at $V_{DC} = 0$.

extracted from the results shown in Fig. 5.4. The same procedure can be applied to the aperiodic fluctuations $\delta G^{d,AB}_{ap.}$ in the AB sample[6] by replacing $A^{UCF}_{ap.}$ with $A^{AB}_{ap.}$ in Eq. 5.18. If we plot as a function of V_{DC} both l_{in}-dependencies normalised to their typical lengths $l_{Th} = \sqrt{\hbar D/eV_c}$ we obtain a similar behaviour (shown by full (■) and open (□) squares in Fig. 5.11) for both samples. Therefore, the aperiodic conductance fluctuations of both the ring and the wire do not show any significant discrepancies and confirm that identical measurements have been performed effectively under non-equilibrium conditions and that the exact geometry of the sample has a negligible influence on the fluctuations, as predicted by Larkin and Khmel'nitskiĭ. Importantly, at high V_{DC}, l_{in} decays as a power law.

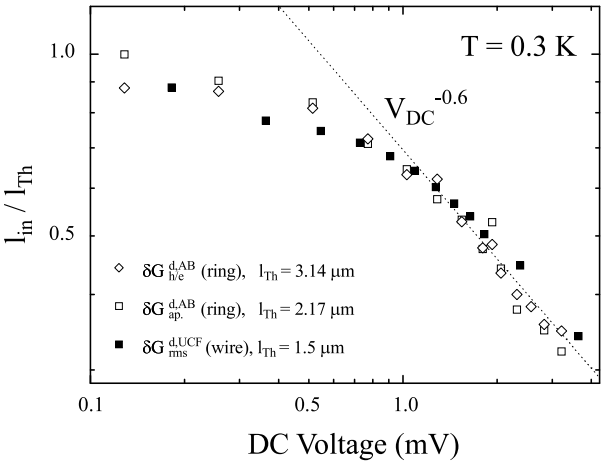

Figure 5.11: Voltage dependence of l_{in} extracted from the measurements $\delta G^{d,AB}_{h/e}$, $\delta G^{d,AB}_{ap.}$ and $\delta G^{d,UCF}_{ap.}$.

A similar analysis can be carried out for the periodic fluctuations.

[6]In the AB sample L is given by the distance between the voltage probes, connected for the half of the ring circumference.

Using the data set $\delta G^{d,AB}_{h/e}$, the expression (similar to Eq. 5.11)

$$\delta G^{d,AB}_{h/e} = A^{AB}_{h/e} \cdot \sqrt{\frac{V_{DC}}{V_c}} \cdot \left(\frac{l_{in}(V_{DC})}{C_r} \right)^{0.65} \cdot \exp\left(-\eta \cdot \frac{C_r}{l_{in}(V_{DC})} \right) \ , \quad (5.19)$$

and the obtained l_{in}/l_{Th} values from $\delta G^{d,AB}_{ap.}$, it is possible to determine $A^{AB}_{h/e}$ and η unequivocally. With these two parameters, $l_{in}(V_{DC})/l_{Th}$ can be extracted from $\delta G^{d,AB}_{h/e}$ (shown as open diamonds ($\Diamond$) in Fig. 5.11) for a check, and it naturally shows the same behaviour as the other l_{in} values found. The result $\eta = 1.1$ is physically reasonable, and $A^{AB}_{h/e} = 0.01$ is close to the values $A^{UCF}_{ap.} = 0.02$, $A^{AB}_{ap.} = 0.04$.

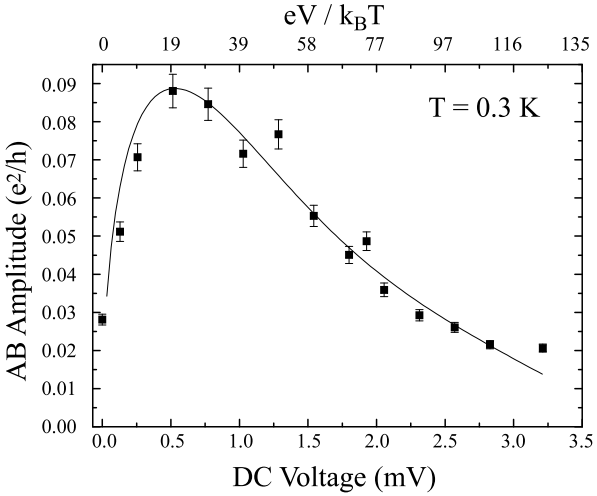

Figure 5.12: AB amplitude as a function of the superimposed DC bias voltage at T=0.3 K, the line is a fit according to formula 5.19.

The exponent q = -0.6 of the dependence $l_{in}/l_{Th} \propto V^q_{DC}$ (Fig. 5.11) inferred from the non-equilibrium measurements can be used to obtain an insight into the source of the decoherence mechanism. A derivation

of the electron-electron dephasing rate as a function of a large applied voltage $eV \gg k_BT$ using a similar method as in [53] gives a dependence $l_\varphi \propto V^{-1/4}$ [54]. The much larger exponent q = -0.6 obtained rules out the electron-electron interaction as the decoherence process and are in favour of the following arguments.

The electronic heating, which affects the effective temperature T_e of the electrons, is known to depend on the voltage when $eV \gg k_BT_{bath}$. More precisely, $T_e \propto V^{2/(2+m)}$ where m is the exponent of the temperature dependence of the contribution of electron-phonon interaction to τ_{in} ($\tau_{e-ph}^{-1} \propto T^m$). This gives $\tau_{in}^{-1} \propto V^{2m/(2+m)}$ or, equivalently, $l_{in}^{-1} \propto V^{m/(2+m)}$. Therefore, l_{in} vs. V_{DC} plots can be used for determination of the exponent m. The result for q = -0.6 gives m = 3. This value of m is large enough that electron-electron interactions as a source of dephasing can be safely ruled out, as expected for such large T_e (of the order 5-12 K for values $V_{DC} \sim$ 2-3 mV). However, m = 3 is too large when one takes into account typical values of $\sim$ 2 - 2.5 obtained in a noise experiment [31] for similar samples. The exponent m depends significantly on the degree of disorder in a sample. For very clean samples and at high temperatures it equals 3, whereas for very dirty sample it has a value of 4. For the samples of intermediate disorder it has lower values, typically 2 - 2.5. The disorder dependence of m is shown in Fig. 5.13. The values of m in the range 2 - 2.5 are probably the realistic ones for our samples.

The present discrepancy is a consequence of the objective sensitivity of m on the exact values of q. For instance, the slope q in Fig. 5.11 can vary between q = -0.55 and q = -0.65. It has to be mentioned that for q = -0.55, m equals exactly 2.5. From the above analysis, it can be argued that the mechanism of decoherence in these samples is due to electron-phonon interaction.

5.7 Aharonov-Bohm oscillations at 3.5 K

The AB experiment has also been carried out at 3.5 K. At such a high temperature oscillations cannot be observed clearly at V_{DC}=0. This is

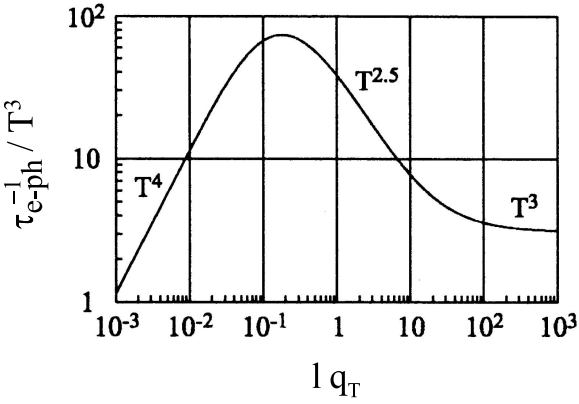

Figure 5.13: Electron-phonon scattering rate as a function of $l \cdot q_T$, which is the wavevector of a phonon with energy $k_B T$ multiplied by the mean free path.

indeed expected, since $k_B T \approx 0.3$ meV, the energy setting up the energy range of interest is much larger than eV_{AC} (see Table 5.3). Suppression of the amplitude ($\propto N^{-1/2} = 1/\sqrt{k_B T/E_c} \approx 1/9$) does not allow to distinguish the periodic oscillations from the noise. However, if V_{DC} is increased oscillations larger than the noise floor can be observed. For $V_{DC} \simeq 0.25$ mV ($eV_{DC} \simeq k_B T$) it is already possible to observe the oscillations (shown in Fig. 5.14 (a)). An enhancement of the oscillation amplitude occurs up to 0.75 mV, and then inelastic processes reduce them. This experiment at $T = 3.5$ K demonstrates clearly that non-equilibrium measurements enable observation of coherence phenomena up to several degrees kelvin, much above the temperatures where equilibrium quantum coherence is found.

5.8 Direct injection of hot electrons

To probe the decoherence of electrons more directly, the following experiment has been done using the sample shown in Fig. 3.7. A *heater*

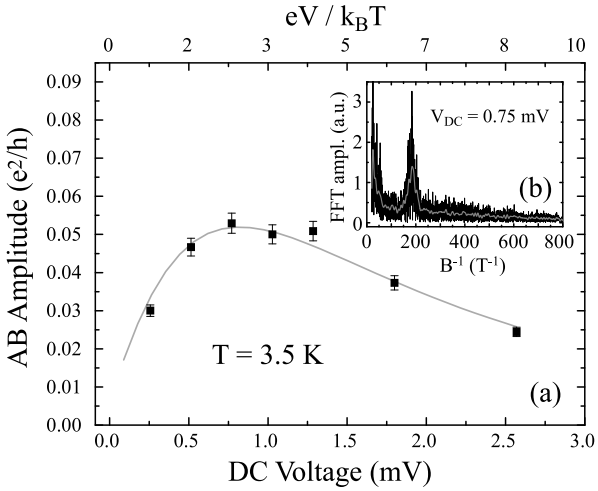

Figure 5.14: AB amplitude as a function of the superimposed DC bias voltage at T=3.5 K, the line serves as a guide for the eye. Inset: Fourier spectrum of the magnetoconductance at $V_{DC} = 0.75\ mV$.

(120 μm long meander line) has been fabricated nearby an AB ring and served as an injector of electrons via a short connection line. The four-terminal resistance of the ring at 300 mK, the temperature at which the experiment was carried out, was 27.8 Ω. The ring was driven out of equilibrium by a constant DC voltage of 0.56 mV superimposed to an AC current of 0.3 μA. The two-terminal resistance of the heater itself was 1.5 $k\Omega$. The heater was heated by a DC current up to 300 μA. This heating leads to injection of hot electrons directly into the ring. The AB amplitude of the ring has been measured as a function of the DC current passing through the heater.

The result (Fig. 5.15 (a)) shows a slow decay of the AB amplitude with increasing the DC current through the heater. Hot electrons coming from the heater enter the ring and are a source of dephasing. Interestingly, if we relate the heater current to the corresponding electron

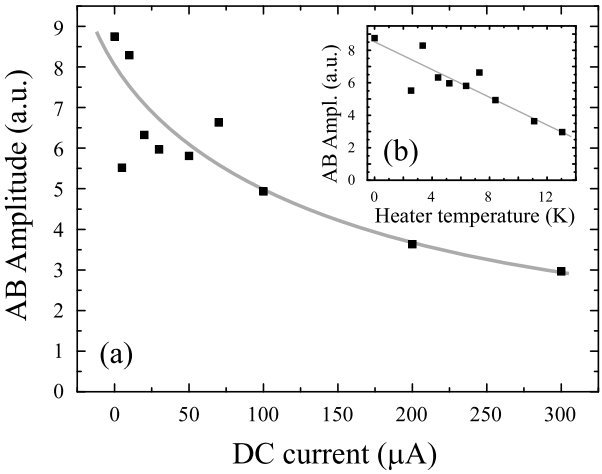

Figure 5.15: (a) AB amplitude behaviour as a function of the DC current passing through the heater. The heater directly injects hot electrons into the ring. (b) AB amplitude as a function of the electron temperature in the heater. The lines serves as a guide for the eye.

temperature according to the formula

$$T_e = \left[T^5 + \frac{1}{\Gamma} \left(\frac{e\mathcal{E}}{k_B} \right)^2 \right]^{1/5} , \tag{5.20}$$

valid for $L \gg l_{e-ph}$, where $\mathcal{E}$ is the electric field and $\Gamma = 5 \cdot 10^9$ K^{-3}m^{-2} the electron-phonon coupling for gold [32], the decrease occurs linearly with the temperature (shown in Fig. 5.15 (b)). Detailed analysis of the AB amplitude is not possible in the present case due to the large width of the ring ($w = 130$ nm) and a corresponding broadening of the Fourier peaks. The width is larger than the AB sample in Fig. 3.6 because of the difficulties to optimise of the line dose in the EBL.

5.9 Summary of the different UCF regimes

In Table 5.4, the formulae which describe the aperiodic fluctuations mentioned in this thesis are summarised. The notation is consistent with that used throughout this thesis. For clarity, the subscript *ap.* has been removed.

Summary of the important formulae

	$V \gg V_c$	$V \ll V_c$
$L < l_\varphi$ $(k_BT \ll eV, eV_c)$	$\Delta I \sim \frac{e^2}{\hbar} V_c \cdot \left(\frac{V}{V_c}\right)^{1/2}$ $\delta G \propto \frac{e^2}{\hbar} \left(\frac{V_c}{V}\right)^{1/2}$ $\delta G^d \propto \frac{e^2}{\hbar} \left(\frac{V}{V_c}\right)^{1/2}$	$\Delta I \sim \frac{e^2}{\hbar} V$ $\delta G \propto \frac{e^2}{\hbar}$ $\delta G^d \propto \frac{e^2}{\hbar}$
$L > l_\varphi$ $(k_BT \ll eV, eV_c)$	$V_\varphi \gg V_c^\varphi$ $\Updownarrow$ $\frac{V}{V_c} \gg \left(\frac{L}{l_\varphi}\right)^3$ $\Delta I_\varphi \sim \frac{e^2}{\hbar} V_c^\varphi \cdot \left(\frac{V_\varphi}{V_c^\varphi}\right)^{1/2}$ $\Delta I \sim \frac{e^2}{\hbar} (V V_c)^{1/2}$ $\delta G \propto \frac{e^2}{\hbar} \left(\frac{V_c}{V}\right)^{1/2}$ $\delta G_\varphi^d \propto \frac{e^2}{\hbar} \left(\frac{V_\varphi}{V_c^\varphi}\right)^{1/2}$ $\delta G^d \propto \frac{e^2}{\hbar} \left(\frac{V}{V_c}\right)^{1/2} \cdot \left(\frac{l_\varphi}{L}\right)^2$	$V_\varphi \ll V_c^\varphi$ $\Updownarrow$ $\frac{V}{V_c} \ll \left(\frac{L}{l_\varphi}\right)^3$ $\Delta I_\varphi \sim \frac{e^2}{\hbar} V_\varphi$ $\Delta I \sim \frac{e^2}{\hbar} V \left(\frac{l_\varphi}{L}\right)^{3/2}$ $\delta G \propto \frac{e^2}{\hbar} \left(\frac{l_\varphi}{L}\right)^{3/2}$ $\delta G_\varphi^d \propto \frac{e^2}{\hbar}$ $\delta G^d \propto \frac{e^2}{\hbar} \left(\frac{l_\varphi}{L}\right)^{1/2}$
$eV_c < k_BT$	$eV_c < k_BT \ll eV$ Thermal averaging is negligible	$eV < eV_c < k_BT$ Thermal averaging is important

Table 5.4: The voltage V corresponds to V_{AC} or V_{DC} depending on the type of a measurement.

Chapter 6

Summary

Conductance G of mesoscopic systems is significantly affected at low temperatures by quantum phenomena. If the size of a sample is of the order of the electron phase-coherence length $l_\varphi(T)$, the wave character of electrons leads to experimentally observable interference phenomena. These are the fluctuations δG of the conductance around its average value $\langle G \rangle$, and can be either aperiodic or periodic. In the former case of universal conductance fluctuations (UCF), the interference pattern is formed as a superposition of the contributions from a continuous range of possible interference paths. Averaged over either impurity configurations, magnetic field or the Fermi energy, the root-mean-square conductance fluctuation $\delta G_{ap.}$ is of the order $\sim e^2/h$. The periodic fluctuations (Aharonov-Bohm or AB effect) are observed if the interference is imposed by the geometry, most commonly in the form of a loop threaded by a magnetic flux ϕ. In this case G is a periodic function of ϕ with a period $\phi_0 = h/e$, and $\delta G_{h/e} \sim e^2/h$. The magnitude of $\delta G_{ap.,h/e}$ can also be affected by an applied voltage V. For the non-equilibrium differential conductance in the regime $V \gg V_c$, the fluctuations amplitude varies as $\delta G^d_{ap.,h/e} \sim (e^2/\hbar)(V/V_c)^{1/2}$, as shown by Larkin and Khmel'nitskiĭ. The validity of the Larkin and Khmel'nitskiĭ theory has been qualitatively confirmed but little attention has been given to the behaviour of $\delta G^d_{ap.,h/e}$ in the regime dominated by inelastic scattering, such as to the suppression of $\delta G^d_{ap.,h/e}$ at very large voltages. In particular, no quanti-

tative description of $\delta G^d_{ap.,h/e}$ in this regime was given nor discussed to what extent the UCF and AB effect can be treated in the same manner when inelastic processes are important. This thesis reports on the non-equilibrium UCF and AB effect in diffusive gold mesoscopic samples, over a wide range of voltages $V \gg k_B T/e, E_c/e$ that cover both the low-voltage $(V/V_c)^{1/2}$ enhancement of $\delta G^d_{ap.,h/e}$ and its suppression at very large voltages. Emphasis is put on the details of the decay of $\delta G^d_{ap.}(V)$ and $\delta G^d_{h/e}(V)$, and it is shown that in the former case the suppression, most probably due to electron-phonon interaction, follows a power law whereas in the latter case the decay is exponential.

Appendix A

Introduction

In the beginning of the work for this thesis a method for fabricating mesoscopic devices (such as nanowires) has been investigated. This approach is based on template synthesis [55] and methods of electrochemistry. It is rather an alternative than a competition to standard EBL [56, 57], because it enables the use of materials which cannot be deposited by evaporation or similar methods.

Arrays of nanowires can be produced by filling a porous membrane containing a large number of straight and narrow cylindrical holes. The filling occurs in a solution by electrochemical deposition [58] (Fig. A.1). Useful templates are, for example, commercially available alumina membranes[1] [59] or track-etched[2] polycarbonate membranes [60].

Realisations using template synthesis appear to be almost limitless, and cover a wide range of applications [61]. For example it allows the fabrication of large assemblies of nearly identical nanowires, ideally suited for measuring magnetic [62, 63, 64] and optical properties [65]. An interesting measurement, namely the conductance measurement made by Cai [66], has attracted our attention, motivated us to investigate transport properties of single conducting polymer (CP) fibers and therefore to develop the alternative template-synthesis approach using electrochemistry.

[1] Anodised aluminium films.

[2] Etched membranes damaged by highly energetic nuclei.

Figure A.1: SEM images of electrochemically grown Ni wires in template after its dissolution (wire length ∼ 6 µm, apparent diameter 100-280 nm).

The work of Cai shows a drastic enhancement of conductivity of chemically template-synthesised polypyrrole and polythiophene nanowires in polycarbonate membranes if smaller pore diameters are employed (Fig. A.2). The conductivity measurements are carried out on an array of fibrils using a two-point measurement method. The polycarbonate membrane filled up with CP is contacted between two electrodes located on each side of the membrane and within a well-defined area. The conductivity of one fibril is deduced by taking into account the membrane's pore density [67].

Unfortunately, this type of measurement is considerably influenced by the contact resistances and the result may not reflect intrinsic properties of CPs. In order to investigate electrical transport properties of a single polymer fiber one has to develop a method for selectively contacting it. This research, done in collaboration with A. Bachtold [68, 69] and M. Krüger [61] is the topic of this Appendix. Two techniques have been investigated and are presented separately in Appendices A.1 and A.2.

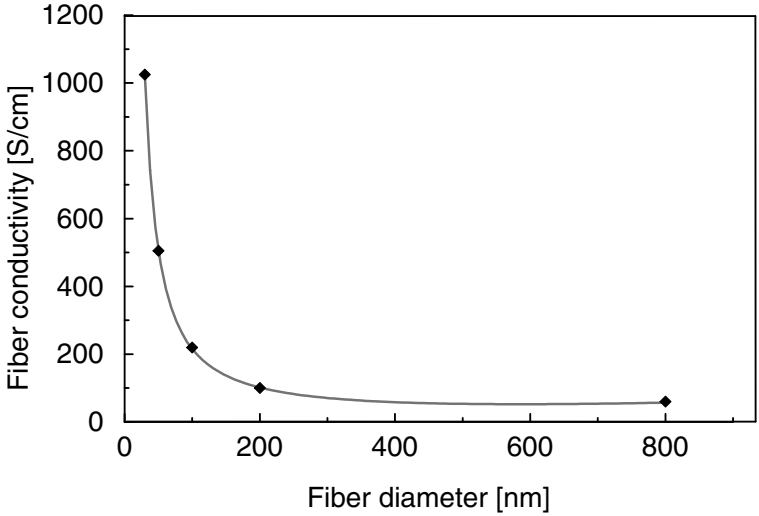

Figure A.2: Conductivity of polypyrrole fibers versus fiber diameter. Polypyrrole is chemically synthesised in polycarbonate membranes with different pore diameters (see [66]).

A.1 Contacting single template synthesised nanowires

In this section a method for making electrical contacts to a few template-synthesised nanowires is presented. The work was performed for Ni wires grown in commercial polycarbonate templates with a nominal pore diameter d_N=80 nm, membrane thickness 6 μm, and mean pore length of 6.5 μm. The mean pore length is larger than the membrane's thickness due to $\pm$ 30° angular distribution of the pore axis [58]. The nominal diameter - characteristic parameter given by the manufacturer - is the pore diameter on the top or bottom of the membrane. Since the pore shows a cigar-like shape [58], the nominal diameter is not a representative value of the average pore diameter. The fabricated contacts enable electrical measurements on a single nanowire as well. The method is a combination of chemical procedures and EBL.

A.1.1 Device fabrication

The average distance between two pores is about 300 nm because of the high pore density of the membrane ($\approx 10^8$ - 10^{10} cm^{-2}). Contacting only one nanowire requires a precise tool such as a high-resolution lithography. But CPs are sensitive to environmental conditions and should certainly not be exposed to a developer. The process was thus designed in a way that the final nanowire is grown during last step, subsequently to *all* lithographic processes.

The different steps in the process are as follows (see Fig. A.3):

- A gold layer, thick enough to close the pores, is deposited on one side of the membrane (typically a 1 cm diameter piece). This layer serves as the bottom electrode for every electrochemical step as well as for electrical measurements.

- Ni is then deposited electrochemically into all pores. As soon as spherical Ni caps start to nucleate on top of the membrane [58], the Ni growth is stopped. This initial filling of the pores protects them during lithographic processes.

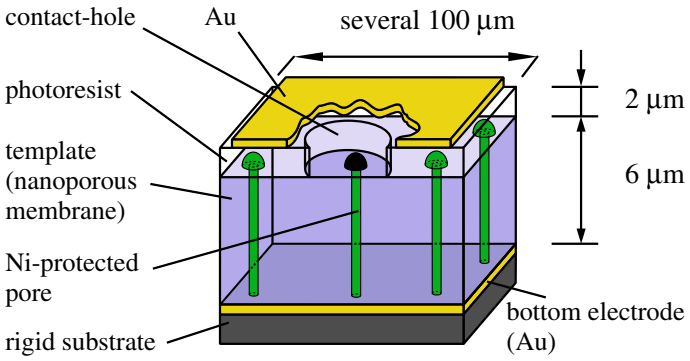

Figure A.3: Schematics (not to scale) showing a completely structured device before the dissolution of the Ni in the pore selected by the contact hole.

- The membrane is fixed onto a rigid substrate with the Au layer facing the substrate, which enables spin coating of a resist layer on top of the Ni caps. Showing a better resistance to chemicals, a positive *Novolak*-based photoresist has been used instead of PMMA.

- Using EBL, a contact hole ($\approx$ 500 nm in diameter) is created[1]. In this process, very few pores can be selected due to the randomness. For a similar protection purpose as mentioned above, Ni electrochemical plating is also used to fill the contact hole (not shown in Fig. A.3).

- The process is completed by making a top electrical contact pad. A 100 nm thick Au layer is evaporated over the whole surface. A second positive resist (PMMA-MA copolymer) is spin-coated and structured using EBL. The structure consists of (a) an opening of $\approx$ 10 μm centred above the previously made contact hole, and (b) open lines separating the central area (several 100 μm) from the rest of the device. Through these openings Au is wet-chemically

[1] Novolak turned out to be usable for EBL as well.

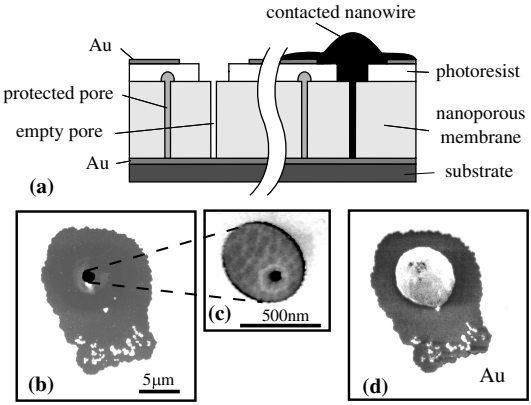

Figure A.4: (a) One selected pore with dissolved Ni protection (left) and refilled with the desired material forming an electric contact to the top Au layer (right). The SEM images are top views of one particular pore after the dissolution of Ni (b), (c) and after (partial) refilling (d).

etched using KI. Finally, the PMMA-MA resist is stripped-off by a commercial remover[2].

Protection of the pores is essential for the success of this method and is maintained during every processing step. At this stage, the protected device can be stored until a final nanowire (such as CP nanowire) is implemented. The preparation of the nanowire is done as follows: the Ni protection is selectively removed through the contact hole by electrochemical dissolution using sulfuric acid (H_2SO_4). The empty pore is then refilled with the material of interest. This time, however, the electrochemical growth is continued until both the pore and the contact hole are filled as well as the gap between the contact hole and the Au pad, as shown in Fig. A.4 (a).

The success of the last filling procedure relies on an important condition: the pore has to be wet at all times, since electrochemistry in

[2] *X AR 600-77/2, Allresist*

dry pores is impossible. It is thus essential to keep the device immersed in a liquid between the electrochemical dissolution and electrodeposition. Fig. A.4 illustrates this last electrochemistry step in which the final nanowire is formed and contacted. The left part of Fig. A.4 (a) shows the dissolution of the pores' Ni protection. In the right part, the same pore has been refilled electrochemically with the material of interest. Once the material has established electrical contact to the gold pad, the filling is stopped. Three SEM snapshots of the same device (Fig. A.4 (b)-(d)) have been taken at different fabrication steps: Fig. A.4 (b) and Fig. A.4 (c) after the dissolution of the Ni protection, and Fig. A.4 (d) after the refilling of the pore (in the present case Ni also).

Figs. A.4 (b) and (c) illustrate the three-level hole hierarchy. The nanopore of the template within a contact hole of 500 nm is shown in Fig. A.4 (c). This contact hole is shown in Fig. A.4 (b), and is located within a ≈ 10 μm large opening of the Au layer. The ragged border of this hole is due to unavoidable Au underetching by the KI stripper. Fig. A.4 (d) demonstrates a successful refilling of the same pore. The bright centred *cap*, which has grown out of the contact hole, is freshly plated Ni. For visualisation purposes the plating is stopped before the Ni could contact the Au surrounding.

A.1.2 Electrical measurements

Since the nanopores are randomly distributed on the surface of a polycarbonate membrane, the number of pores being selected by an arbitrarily placed contact hole remains unknown. In order to measure intrinsic electrical resistance of nanowires formed by template synthesis, the number of contacted nanowires has to be determined. Therefore a statistical analysis of the measured conductance G must be carried out.

In Fig. A.5 (a) the conductances of 30 identically prepared devices are shown. The devices consist of pores filled with Ni and were measured at $T = 300$ K. Each point corresponds to one device. The horizontal axis, representing an arbitrary device number, has been arranged in such a way that the G-values appear in ascending order. Sharp steps would appear if all the devices could be considered as identical ones (see Sec-

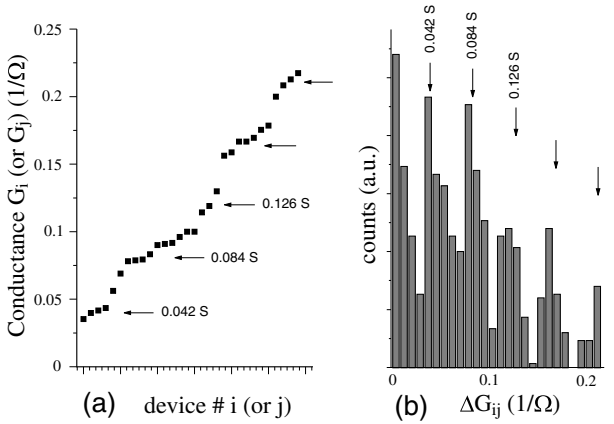

Figure A.5: (a) Conductance values for 30 *devices with Ni wires represented in ascending order. (b) Histogram of the difference in conductance for different devices.*

tion A.1.3). However, we rather notice an accumulation of points around the particular G-values of 0.042 S, 0.084 S, and 0.168 S (represented by arrows in Fig. A.5 (a)). Since conductance values $G \leq 0.03$ S have not been found, it can be deduced that the conductance $G \approx 0.042$ S probably corresponds to one single nanowire. This nanowire-conductance *unit* can be more accurately derived from the histogram shown in Fig. A.5 (b), which represents the difference in conductance ($\Delta G_{ij} = |G_i - G_j|$) for two different devices, obtained by taking all possible combinations ij ($i \neq j$) of the 30 measured devices. The histogram shows pronounced equidistantly spaced peaks. In this case, the average distance between the peaks represents the mean conductance for one single nanowire, $G = (23\ \Omega)^{-1}$. Using the measured specific resistance of ρ= 7.7 $\mu\Omega$cm for electroplated Ni films, the average inner pore diameter[3] of 160 nm, and the mean pore length of 6.5 μm, a single Ni wire should have an average resistance of 25 Ω, in excellent agreement with the present experiment. This result

[3]See explanations in Section A.1

also proves that the contact resistances are negligible for Ni-wires with nominal pore diameter[3] of d_N=80 nm.

A.1.3 Conclusion and comments

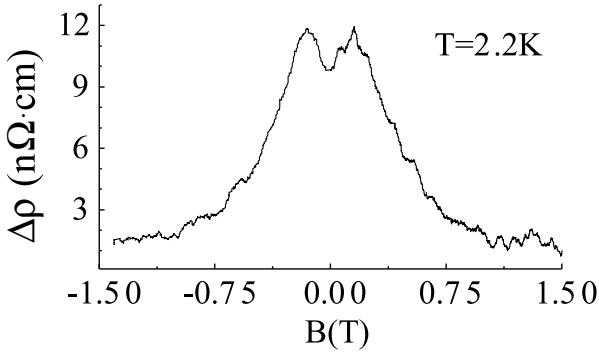

Figure A.6: Magnetoresistance of 4 contacted Ni nanowires measured at $T = 2.2\,K$ with the magnetic field B directed $\perp$ to the Ni nanowire.

Conducting nanowires were electrochemically fabricated in templates consisting of a large and dense array of nanopores. Electrical contacts to a single or few nanowires were successfully made by combining chemical methods and high-resolution EBL in a multi-level process. Electrical measurements on a set of nanowire devices demonstrate that the conductance of one single nanowire can be determined by means of a statistical analysis. After this analysis the devices with only one contacted Ni wire may be used further, for example, to grow alternative materials such as Bi and CPs after successful dissolution of the Ni. Fig. A.6 shows a first magnetoresistance measurement, demonstrating that the nanowires, contacted according to the description given above, can be used for studies of electrical transport at low temperatures. Although this method promises interesting possibilities, the following problems have been identified:

- The fabricated contact hole cannot be self-aligned to only one pore in a straightforward way.

- Attaching macroscopic wires to the Au contact pads by ultrasonic bonding is almost impossible, most probably because of the polycarbonate membrane's softness.

- In order to obtain intrinsic unambiguous electrical properties, four-terminal measurements are necessary. The multi-level fabrication procedure is not suitable for creating a simple four-terminal device.

- Volumes of the pores are not known a priori: the pore diameter is not constant along the pore axis (as shown in Ref. [58]) and thus the specification of the manufacturer is not accurate enough. In order to determine the resistivity from the measured resistance, an extensive investigation of the geometry has to precede electrical measurements for each new pore diameter.

- Because of incompatibility of the organic solvents and resists, the method has been applicable only for polypyrrole wires, which can be synthesised in an aqueous solution.

Growth of polypyrrole (see Ref. [61] for synthesis parameters) nanowires was tried. The Au pad was sometimes covered by polypyrrole (shown in Fig. A.7), but the resistance could not be measured reliably. For eight different devices, resistances of 50 Ω, 710 Ω, 2.2 kΩ, 2.4 kΩ, 3.9 kΩ, 4.3 kΩ, 1.38 MΩ, 6 MΩ and 12 MΩ were respectively obtained. Taking the best values for the conductivity of polypyrrole and the geometrical shape into account, one would expect nanowires to have resistances in the range of 42-43 kΩ. The low resistance values are probably due to the shortcuts with non-fully-dissolved Ni nanowires. It is not easy to obtain reliable contacts to electrochemically grown CP wires. Furthermore, it is difficult to carry out a statistical analysis because the reported bulk conductivity values for CP (see [61]) differ from source to source. The fabrication of the devices is also very time-consuming. For these reasons an alternative contacting method for enabling four-terminal measurements, together with a better control of the wire formation, was developed. A

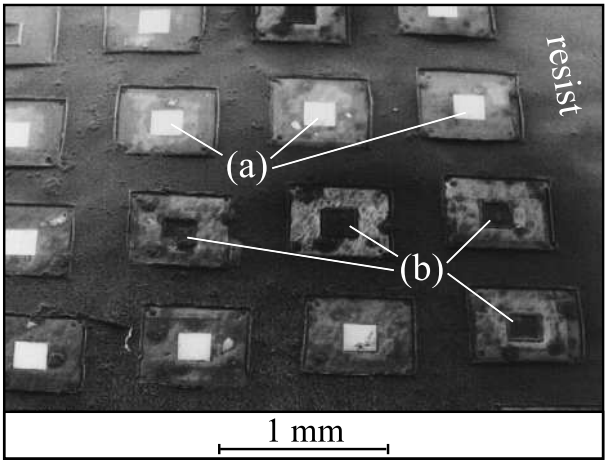

Figure A.7: SEM image (topview) of an array of different devices after dissolution of the Ni-wire and electro-polymerisation of polypyrrole. No reliable resistances could be measured. (a) Au-pads. (b) In some cases, polypyrrole was grown on top of the Au-pads.

self-made template laterally aligned to the surface in a polyimide resist replaced the track-etched pores. This approach is described in the next section.

A.2 Template fabrication of lateral nanopores in polyimide

A.2.1 Method

Since surface-structuring techniques are rather well known and offer a better control for achieving reliable electrical contacts, making use of them (instead of a multi-level technique) may be more appropriate for template-synthesis purposes. Furthermore, devices produced in this manner might have higher stability against mechanical stress, and interconnects or branched networks could be readily created. This is a method which has been investigated after having identified the problems mentioned in Section A.1.3.

Four macroscopically thick Au pads are structured on top of a Si/SiO_2 chip[1] by optical lithography (see Section B.1 for details) and used as bond pads in a later step. The device configuration is shown schematically in Fig. A.8 (a) (top-view) and Fig. A.8 (b) (cross-section). The outer left and right pads are used as current contacts, whereas the two inner *fingers* (Fig. A.9) are used for measuring the voltage drop, thereby creating a true four-terminal device. It should also be mentioned that the two Au fingers are optional and can be omitted for a two-terminal configuration or replaced by other terminals (such as a gate) upon requirement. If necessary, these fingers are connected to the Au pads by EBL and Au evaporation. In the next step a lateral pore is created by EBL and three-angle technique evaporation in order to overcome the high step between the Au pads and the substrate. The required shape between the left and right Au pads is defined by a Ni (or Cu) *mold* structure (see Fig. A.9). The Ni mold wires are usually 100-200 nm wide, 100 nm thick and 6 μm long.

Then a polyimide layer is spin-coated over the whole device (see Section B.2) and serves as a template. Finally, on one side of the device a large opening[2] was structured in the polyimid template using lithography and reactive ion etching (RIE) (see Section B.3) in an additionally

[1] 1.5 cm $\times$ 2 cm in size.
[2] 400 μm $\times$ 400 μm in size.

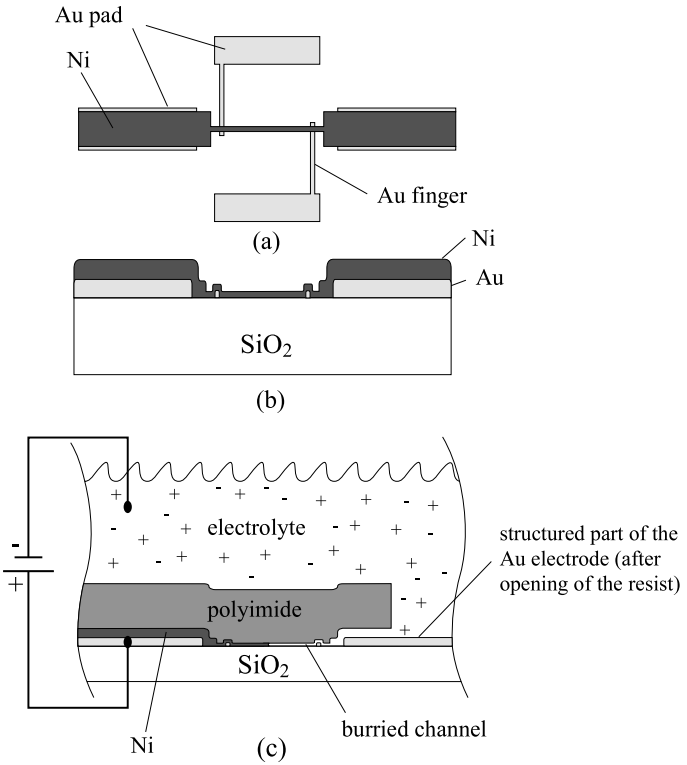

Figure A.8: (a) Top-view of a particular device configuration designed for four-terminal electrical measurements. (b) Cross section of the device described in (a). (c) The device is covered by polyimide. The Ni is electrochemically dissolved, which results in a lateral nanochannel between the two Au contacts.

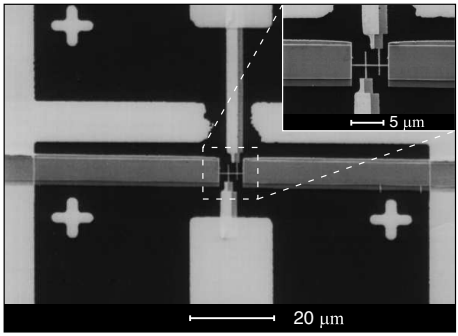

Figure A.9: SEM image of a Ni mold nanowire fabricated over two gold fingers. At this stage, the polyimide resist used as template is not spin-coated yet.

spun, sacrificial resist layer[3]. The Ni mold is dissolved electrochemically and/or chemically[4] through this opening. This results in a *lateral nanochannel* underneath the polyimide insulating layer, as shown in Fig. A.8 (c). It is somewhat difficult to control the effects of the mixture of acids on the dissolution. Fortunately, the polyimide resist has shown a appreciable resistance against any chemicals used (such as acids or organic solvents) as well as a good mechanical stability and it is thus not affected by the concentration and composition variations.

The nanochannel connects the Au pads and ends in the opening, thus enabling an other electrochemical solution to fill it in completely. Electrochemistry of a CP or any other material can now take place. A successful electrochemical dissolution of Ni can be seen in Fig. A.10, showing a single lateral pore in formation.

[3]Both EBL in PMMA or UV lithography with optical alignment procedure are possible.

[4]By a 1:5 mixture of H_2SO_4 (98%) / H_3PO_4 (42%).

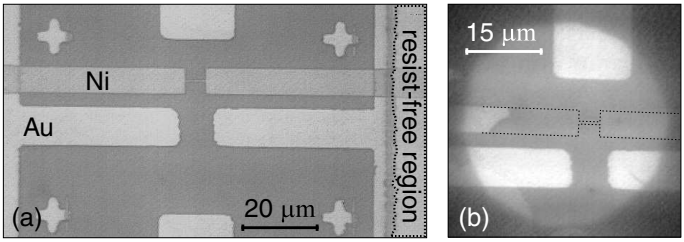

Figure A.10: (a) Optical microscope image of a Ni mold nanowire joining two Au pads and covered by an inert polyimide resist. On the right side an opening in the polyimide resist is shown. (b) Optical microscope image of a lateral channel in formation (indicated by dotted lines) due to the electrochemical dissolution of the Ni.

A.2.2 Experimental results and discussion

Following the success of the above-mentioned lateral nanochannels, it was necessary to test their usefulness for electrical measurements on electroplated CPs. For this purpose, and for simplicity, two-terminal devices were fabricated. After the dissolution, the nanochannels were kept wet (in pure water) and finally mounted into an electrochemical cell with the plating bath of interest [61]. It was found that several CP wires[5], as well as Bi wires, could be synthesised (see [61]) in the nanochannels. For instance, Fig. A.11 (a) shows a successful refilling of the pore with Bi (optical microscope image). Because of a relatively thick insulating layer (2-3 μm of polyimide), a precise SEM imaging is not achievable here. Bi-magnetoresistance curves have been measured at three different temperatures and are shown in Fig. A.11 (b).

The filling of a pore with CPs is difficult to observe by either simple optical microscopy or confocal optical microscopy. The success of this step with CPs is thus unclear. Sometimes the polymer wires grew out of the pores and covered the contact pad. As shown in Fig. A.12 (b), it is not clear whether the CP has grown homogeneously inside the channel.

[5]Poly-3-methyl-thiophene, polypyrrole or polythiophene.

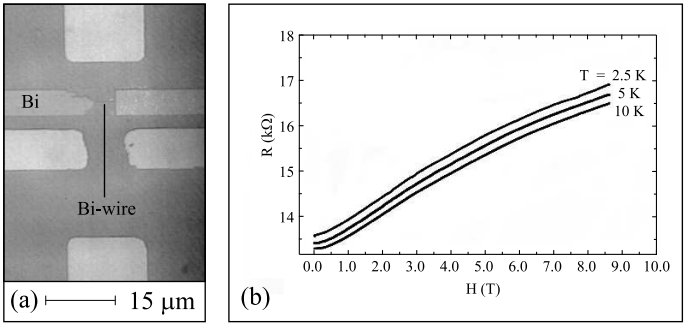

Figure A.11: (a) Optical-microscope image of a Bi wire obtained by the template synthesis in a single pore fabricated in-plane before. (b) Magnetoresistance of such a wire at three different temperatures.

A quite sharp contour might indicate that the Ni wire may not have been completely dissolved, but the "black material" (see the left Au pad and the opening on the right, Fig. A.12 (b)) has surely been deposited. The "black material" is presumably the polymer. A chip with 5 nanochannels is shown in Fig. A.12 (a).

In conclusion, the laterally-grown pores can be filled with CP. Resistance measurements have been carried out successfully, but they show relatively high values of a few MΩ. The *I-V* characteristic exhibits a non-ohmic behaviour. Taking the geometrical factor into account, a conductivity below 1 S/cm has been deduced (70-120 S/cm corresponds to bulk conductivity of a CP film). It was not clear whether the measured conductivity was linked to the polymer itself or maybe to the ionic solution remaining in the pore. The low conductivity value could be explained by the type of measurement applied (2-terminal), since the contact resistances might play an important role. It should also be noted that the growth of CPs on SiO_2 is different than the growth used for bulk film characterisation [61]. As such, the overall physical properties can be different and the conductivity can be significantly affected by that difference.

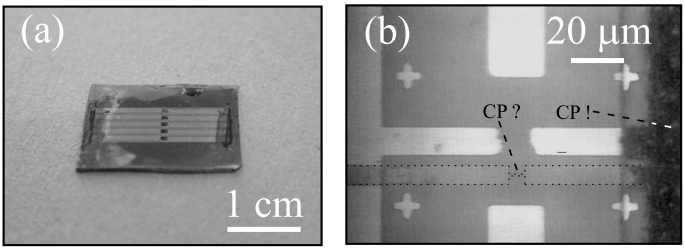

Figure A.12: (a) Optical image of 5 aligned devices on top of a silicon chip. The openings in the polyimide resist can be seen very clearly as small black squares. The black colour let us suppose that CP has grown out of the channel. (b) Optical microscope image of the inner part of such a device.

Four-terminal channels filled with CP have still not been successfully produced. After the dissolution of the Ni mold structure, attempts to grow CPs in the resulting channel failed. The CP was growing in the channel as well as in between the polyimide template and the finger structure (Fig. A.9) used as voltage probes, indicating the presence of an unwanted free space. Unavoidable shortcuts between this free space and the CP plating bath dashed our hopes for a success in making such a four-terminal device in a reasonably short period of time.

In the meantime other CPs (carbon nanotubes) have been discovered, produced and identified as promising candidates for further studies [8, 61, 70, 71, 72, 73, 74], which slowly stopped the work on the project presented in Appendices A.1 and A.2. However, the usefulness of this research is still present, because numerous subtle experimental procedures used later by the author and other co-workers originate from this activity (such as [61]). Even if this project has been stopped regarding our group's interests and goals, it seems that research is still going on using such presented techniques [75, 76], where carbon nanotubes were synthesised in template by chemical vapour deposition (CVD).

Appendix B

Detail of structuring methods

B.1 UV lithography

The principles of UV lithography are basically the same as those of EBL. A pattern is transferred into a resist, which is developed by a chemical procedure. However, the pattern is not defined by the movements of an electron-beam but rather by the exposure to UV light, which passes through a chromium mask.

For the experiments described in this work the following procedure has been applied: after the cleaning of a substrate (ozone oven → ultrasonic IPA bath → ultrasonic ethanol bath → pure water), HMDS[1] is spin-coated at 2000 rpm for 40 s. HMDS modifies the hydrophilic SiO_2 surface into a hydrophobic one, which results in a better adhesion of the resist. A $\sim$ 2 μm thick *ma-N-420* [2] negative resist is then spun and baked at 87.5°C for 30 min. Lithography is performed by a 1 - 1.5 min of exposure to UV produced by a mercury lamp (*Maskaligner MJB 3*, *Karl Suss*). The development is done in a *ma-D-332* developer solution for 20-25 min.

[1] Hexamethyldisilazane.
[2] Micro resist technology, Germany.

B.2 Spin coating and baking of polyimide

Polyimide resist *PI 2570* is commercially available from the company *DuPont*. The spin-coating sequence is described by Fig. B.1. A specific baking process was chosen in order to possibly get the most inert polyimide (Table B.1). The polyimide produced by this method is 2.7 to 3 μm thick.

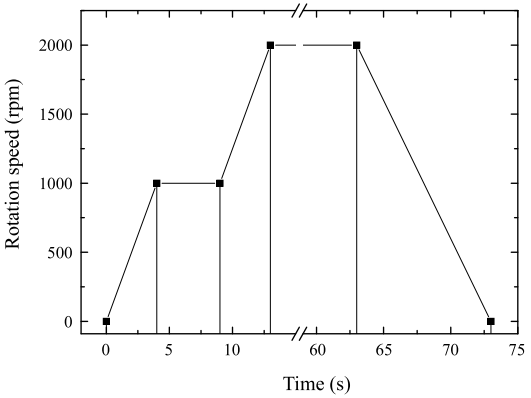

Figure B.1: Spin-coating procedure for polyimide.

Step	Time	Temperature
Prebaking (air)	0 - 50 min 50 - 80 min 80 - 140 min	20 - 200°C 200°C 200 - 350°C
Hard baking (N_2 atm.)	140 - 200 min	350°C
Cooling (N_2 atm.)	overnight	350 - 20°C

Table B.1: Hard baking procedure.

B.3 Dry plasma etching

In microstructuring, it is often necessary to use subtractive methods for transferring a lithographically created pattern onto a substrate. This can be done by dry plasma etching, either physically (using heavy-ion bombardment, such as Ar^+), or chemically (using reactive ions, like fluorine or chlorine). As outlined below, one can distinguish different etching methods with respect to the etching process involved and parameters such as selectivity, anisotropy, uniformity, etch rate, etc.

- Dry chemical etching, which involves chemical reactions, is an isotropic and selective method.
- Reactive ion etching (RIE), or ion-enhanced etching, involves both physical and chemical processes, is anisotropic and selective. This method enables higher etch selectivity between the resist mask and the material to be etched.
- Ion milling, or sputter etching (see also Section 3.3), is based on physical processes, is anisotropic and non-selective. This method is appropriate if a surface has to be cleaned mechanically or if a chemically inert material, such as a noble metal, has to be structured.

For the etching of polyimide, described in Section A.2.1, RIE with a CHF_3 / O_2 = 1:3 plasma (100 W and 0.05 mbar of base pressure) was carried out for ∼20 min. The thickness of remaining polyimide was 1 - 1.5 μm.

Bibliography

[1] G. P. Lopinski, D. D. M. Wayner, and R. A. Wolkow, Nature **406**, 48 (2000).

[2] Y. Aharonov and D. Bohm, Phys. Rev. **115**, 485 (1959).

[3] B. L. Al'tshuler, A. G. Aronov, and B. Z. Spivak, JETP Lett. **33**, 272 (1982).

[4] C. P. Umbach, S. Washburn, R. B. Laibowitz, and R. A. Webb, Phys. Rev. B **30**, 4048 (1984).

[5] R. A. Webb, S. Washburn, C. P. Umbach, and R. B. Laibowitz, Phys. Rev. Lett. **54**, 2696 (1985).

[6] B. Pannetier, J. Chaussy, R. Rammal, and P. Gandit, Phys. Rev. Lett. **53**, 718 (1984).

[7] V. Chandrasekhar, M. J. Rooks, S. Wind, and D. E. Prober, Phys. Rev. Lett. **55**, 1610 (1985).

[8] A. Bachtold *et al.*, Nature **397**, 673 (1999).

[9] P. W. Anderson, Phys. Rev. **109**, 1492 (1958).

[10] P. A. Lee, A. D. Stone, and H. Fukuyama, Phys. Rev. B **35**, 1039 (1987).

[11] A. I. Larkin and D. E. Khmel'nitskiĭ, Sov. Phys. JETP **64**, 1075 (1986).

[12] Y. V. Sharvin and N. I. Bogatina, Sov. Phys. JETP **29**, 419 (1969).

[13] S. Datta, *Electronic transport in mesoscopic systems* (Cambridge University Press, Cambridge, 1995).

[14] G. Bergmann, Phys. Rev. B **28**, 2914 (1983).

[15] A. I. Larkin and D. E. Khmel'nitskiĭ, Sov. Phys. Usp. **25**, 185 (1982).

[16] D. E. Khmel'nitskiĭ, Physica **126B**, 235 (1984).

[17] G. Bergman, Solid State Comm. **42**, 815 (1982).

[18] P. A. Lee and A. D. Stone, Phys. Rev. Lett. **55**, 1622 (1985).

[19] J. C. Licini, D. J. Bishop, M. A. Kastner, and J. Melngailis, Phys. Rev. Lett. **55**, 2987 (1985).

[20] D. Y. Sharvin and Y. V. Sharvin, JETP Lett. **33**, 272 (1982).

[21] A. G. Aronov and Y. V. Sharvin, Rev. Mod. Phys. **59**, 755 (1987).

[22] M. Gijs, C. van Haesendock, and Y. Bruynseraede, Phys. Rev. Lett. **52**, 2069 (1984).

[23] C. P. Umbach *et al.*, Phys. Rev. Lett. **56**, 386 (1986).

[24] A. D. Stone and Y. Imry, Phys. Rev. Lett. **56**, 189 (1986).

[25] E. Scheer *et al.*, Phys. Rev. Lett. **78**, 3362 (1997).

[26] P. Mohanty, Physica B **280(1-4)**, 446 (2000).

[27] A. D. Zaikin and D. S. Golubev, Physica B **280 (1-4)**, 453 (2000).

[28] B. L. Al'tshuler, A. G. Aronov, D. E. Khmel'nitskiĭ, and A. I. Larkin, *Quantum Theory of Solids (p.130)* (Mir Publishers Moscow, Moscow, 1982).

[29] R. P. Feynman, *Lectures on Physics (Section 1-1)* (Addison-Wesley, New-York, 1965), Vol. III.

[30] P. Dubos *et al.*, J. Vac. Sci. Technol. B **18**, 122 (2000).

[31] M. Henny, Ph.D. thesis, University of Basel (Switzerland), 1998.

[32] M. Henny *et al.*, Appl. Phys. Lett. **71**, 773 (1997).

[33] C. Terrier *et al.*, Fizika A (Zagreb) **8-3**, 157 (1999).

[34] T. Hoss, Ph.D. thesis, University of Basel (Switzerland), 2000.

[35] C. W. J. Beenakker and H. van Houten, *Solid State Physics; Advances in Research and Applications* (Academic, New-York, 1991), Vol. 44.

[36] S. Washburn and R. A. Webb, Rep. Prog. Phys **55**, 1311 (1992).

[37] B. L. Al'tshuler, JETP Lett. **41**, 648 (1985).

[38] B. L. Al'tshuler and D. E. Khmel'nitskiĭ, JETP Lett. **42**, 359 (1985).

[39] R. A. Webb, S. Washburn, and C. P. Umbach, Phys. Rev. B **37**, 8455 (1988).

[40] D. C. Ralph, K. S. Ralls, and R. A. Buhrman, Phys. Rev. Lett. **70**, 986 (1993).

[41] R. Schäfer, K. Hecker, H. Hegger, and W. Langheinrich, Phys. Rev. B **53**, 15964 (1996).

[42] R. Häußler, Ph.D. thesis, Universität Karlsruhe (Germany), 1999.

[43] F. P. Milliken *et al.*, Phys. Rev. B **36**, 4465 (1987).

[44] D. P. DiVincenzo and C. L. Kane, Phys. Rev. B **38**, 3006 (1988).

[45] S. Chakravarty and A. Schmid, Phys. Rep. **140**, 193 (1986).

[46] A. Stern, Y. Aharonov, and Y. Imry, Phys. Rev. A **41**, 3436 (1990).

[47] R. Landauer, Philos. Mag. **21**, 863 (1970).

[48] V. Chandrasekhar, P. Santhanam, and D. E. Prober, Phys. Rev. B **44**, 11203 (1991).

[49] B. L. Al'tshuler and A. G. Aronov, JETP Lett. **33**, 499 (1981).

[50] S. Washburn, C. P. Umbach, R. B. Laibowitz, and R. A. Webb, Phys. Rev. B **32**, 4789 (1985).

[51] M. Henny, S. Oberholzer, C. Strunk, and C. Schönenberger, Phys. Rev. B **59**, 2871 (1999).

[52] F. C. Wellstood, C. Urbina, and J. Clarke, Phys. Rev. B **49**, 5942 (1994).

[53] A. B. Gougam *et al.*, J. Low Temp. Phys. **118**, 447 (2000).

[54] D. Babić, private communication, 2000.

[55] C. R. Martin, Science **266**, 1961 (1994).

[56] H. I. Smith and H. G. Craighead, Physics Today **24**, February (1990).

[57] P. Vettiger, U. Staufer, and D. P. Kern (eds.), Microelectronic Eng. **32**, September (1996).

[58] C. Schönenberger *et al.*, J. Phys. Chem. B **101**, 5497 (1997).

[59] R. C. Furneaux, W. R. Rigby, and A. P. Davidson, Nature **337**, 147 (1989).

[60] R. L. Fleischer, P. B. Price, and R. M. Walker, *Nuclear Tracks in Solids* (Univ. of California Press, Berkeley, 1975).

[61] M. Krüger, Ph.D. thesis, University of Basel (Switzerland), 2000.

[62] D. AlMawlawi, N. Coombs, and M. Moskovits, J. Appl. Phys. **70**, 4421 (1991).

[63] T. M. Whitney, J. S. Jiang, P. C. Searson, and C. L. Chien, Science **261**, 1361 (1993).

[64] J. Meier, B. Doudin, and J.-P. Ansermet, J. Appl. Phys. **79**, 6010 (1996).

[65] B. M. I. van der Zande, M. R. Böhmer, L. G. J. Fokkink, and C. Schönenberger, J. Phys. Chem. B **101**, 852 (1997).

[66] Z. Cai and C. R. Martin, J. Am. Chem. Soc. **111**, 4138 (1989).

[67] Z. Cai *et al.*, Chem. Mater. **3**, 960 (1991).

[68] A. Bachtold, Ph.D. thesis, University of Basel (Switzerland), 1999.

[69] A. Bachtold *et al.*, Microelectronic Engineering **41/42**, 571 (1998).

[70] M. Krüger *et al.*, cond-mat/0009171, 2000.

[71] C. Schönenberger and L. Forró, Physics World **13-6**, 37 (2000).

[72] C. Strunk, A. Bachtold, T. Nussbaumer, and C. Schönenberger, Physica B **280**, 384 (2000).

[73] C. Schönenberger, A. Bachtold, C. Strunk, and J.-P. Salvetat, Appl. Phys. A **69**, 283 (1999).

[74] A. Bachtold *et al.*, Appl. Phys. Lett. **73**, 274 (1998).

[75] J. Li, C. Papadopoulos, and J. M. Xu, Nature **402**, 253 (1999).

[76] C. Papadopoulos *et al.*, Phys. Rev. Lett. **85**, 3476 (2000).

List of publications

Publications in journals and proceedings

- *The amplitude of non-equilibrium quantum interference in metallic mesoscopic systems*, C. Terrier, D. Babić, C. Strunk, T. Nussbaumer and C. Schönenberger, to appear in Europhysics Letters, 2002

- *Amplitude of Aharonov-Bohm oscillations in mesoscopic metallic rings as a function of the DC bias voltage*, C. Terrier, T. Nussbaumer, C. Strunk, D. Babić, and C. Schönenberger, Fizika A **8(3)**, 157-164, 1999

- *Contacting carbon-nanotubes selectively with low-ohmic contacts for four-probe electric measurements*, A. Bachtold, J.-P. Salvetat, J.-M. Bonard, M. Henny, C. Terrier, C. Strunk, L. Forró, and C. Schönenberger, Appl. Phys. Lett. **73**, 274-276, 1998

- *Contacting single template synthesised nanowires for electric measurements*, A. Bachtold, C. Terrier, M. Krüger, M. Henny, T. Hoss, C. Strunk, R. Huber, H. Birk, U. Staufer, and C. Schönenberger, Microelectronic Engineering **41/42**, 571, 1998

- *Stress-induced anisotropy in* $Fe_{0.50}Co_{0.48}V_{0.02}$ *coatings for neutron beam polarization*, D. Clemens, A. Vananti, C. Terrier, P. Böni, M. Senthil Kumar and M. Horisberger, J. Magn. Magn. Mater. **177-181**, 1237-1238, 1998

- *Magnetic in-plane anisotropy in sputtered FeCo films and multilayers*, D. Clemens, A. Vananti, C. Terrier, P. Böni, B. Schnyder, S. Tixier, M. Horisberger, Physica B **234-236**, 500, 1997

Talks

- *Non-equilibrium coherent transport in mesoscopic conductors*, Ph.D. defense, 21^{th} of December 2000, University of Basel, Switzerland

Poster contributions

- *Non-equilibrium quantum interference in metallic mesoscopic systems*, C. Strunk, C. Terrier, D. Babić, T. Nussbaumer and C. Schönenberger, The 23rd International Conference on Low Temperature Physics, Hiroshima, Japan, 20-27 Aug. 2002

- *Wire-Like Molecules as Electrical Conductors*, A. Bachtold, D. Babić, M. Buitelaar, F. Dewarrat, M. Calame, H.-W. Fink, K. Furukawa, M. Iqbal, M. Krüger, T. Nussbaumer, C. Strunk, C. Schönenberger and C. Terrier, NFP36 National Science Program on Nanoscience, Bern, Switzerland, 14 Nov. 2000

- *Non-equilibrium coherent transport in mesoscopic conductors*, C. Terrier, D. Babić, C. Strunk, T. Nussbaumer and C. Schönenberger, Mesoscopic Electronics, Ascona, Switzerland, 9-13 October 2000

- *Amplitude of Aharonov-Bohm oscillations in mesoscopic metallic rings as a function of the DC bias voltage*, C. Terrier, C. Strunk, T. Nussbaumer, D. Babić and C. Schönenberger, EPS/CMD18-2000, Montreux, Switzerland, 13-17 March 2000

- *Towards electrical transport experiments in single polymer nanowire*, C. Terrier, M. Krüger, A. Bachtold and C. Schönenberger, 3^{rd} Workshop on Nanoscience, Hasliberg, Switzerland, Oct. 1998

- *Towards electrical transport experiments in single polymer nanowire*, C. Terrier, M. Krüger, A. Bachtold and C. Schönenberger, International Summer School on Nanophysics, Helsinki, Finland, Aug. 1998, **Best Poster Award**

- *Contacting single template-synthesised nanowires for electric measurements*, C. Terrier, A. Bachtold, M. Krüger and C. Schönenberger, Micro- and Nanoengineering MNE 97, Athens, Greece, 15-18 Sept. 1997

Curriculum Vitæ

Christophe Terrier

14 avril 1973	Né à Porrentruy, originaire de Montignez (JU)
1979 - 1983	Ecole primaire Bassecourt
1983 - 1988	Ecole secondaire Bassecourt
1988 - 1991	Lycée cantonal Porrentruy Maturité type C
1991 - 1996	Ecole polytechnique fédérale Zurich
1992	Premiers examens propédeutiques
1993	Seconds examens propédeutiques
1996	Diplôme en physique expérimentale Spécialisation en physique du solide Travail de diplôme dans le groupe du Prof. Dr. A. Furrer (Institut Paul Scherrer), *Anisotropie magnétique dans des multicouches de* $[TiN/FeCoV]_x$
1997 - 2000	Thèse de doctorat sous la supervision du Prof. Dr. C. Schönenberger, *Non-Equilibrium Coherent Transport in Mesoscopic Conductors* Assistant et coordinateur pour les cours "Physik I" et "Physik II"
21.12.2000	Soutenance de thèse

Professeurs ayant contribué à ma formation scientifique:

C. Blatter, G. Blatter, J. Brunner, R. E. Bühler, P. Embrechts, H.-W. Fink, A. Furrer, H. J. Gerber, G. Gonnet, W. Hunziker, W. Kröger, O. E. Lanford III, J. Lang, C. Lubich, W. Lukosz, A. C. Mota, H. R. Ott, T. M. Rice, C. Schmid, C. Schönenberger, H.-C. Siegmann, C. Strunk, E. Trubowitz, G. Yadigaroglu.

Remerciements

Par ces quelques lignes, j'aimerais remercier, sans distinction aucune, toutes les personnes qui m'ont aidé ou soutenu dans ma thèse de doctorat et ont ainsi participé à sa réussite. Dinko Babić, Christoph Strunk et mon professeur de thèse Christian Schönenberger pour l'esprit et la disponibilité qu'ils affichent, pour l'exemple, la motivation qu'ils transmettent ainsi que pour tout le travail de supervision qu'ils ont effectué pour cette présente thèse. Je leur en suis gré et reconnaissant et les remercie aussi pour leur collégialité et leur amabilité.

Par la même occasion, j'aimerais citer et remercier tous mes collègues, anciens ou actuels membres du groupe *Schönenberger*, qui contribuent et ont contribué par leurs différentes idées, points de vue, cultures, échanges, aide, à une ambiance amicale, saine, décontractée et prospère: Jan Aarts, Adrian Bachtold, Holger Birk, Mark Buitelaar, Michel Calame, Bong-Ryoul Choi, François Dewarrat, Hans-Werner Fink, Jürg Furer, Kazuaki Furukawa, Matthias Henny, Tilman Hoss, Richard Huber, Mahdi Iqbal, Michael Krüger, Thomas Nussbaumer, Stefan Oberholzer et Urs Staufer. J'associe à mes collègues Eugene Sukhorukov pour ses conseils théoriques.

J'aimerais aussi adresser mes remerciements à certaines personnes dites "de l'ombre", personnes sans lesquelles le fonctionnement d'un institut de physique serait peut-être remis en question, à savoir mécaniciens, techniciens, electroniciens, secrétaires, et parmi elles, Paul Cattin, Astrid Kalt, Barbara Kammerman, Daniel Michel et Werner Roth.

J'aimerais enfin exprimer mes remerciements à mes parents, frère et soeur, à tous les amis que j'ai cotoyés durant ces quelques années de thèse, ainsi qu'à Rob Jubbenville pour son aide dans la correction de ce

document.

Cette thèse de doctorat a été financée par le Fond National Suisse pour la Recherche.